

**NASA TECHNICAL  
MEMORANDUM**

**NASA TM 73720**

(NASA-TM-73720) A HIGH PRESSURE MODULATED  
MOLECULAR BEAM MASS SPECTROMETRIC SAMPLING  
SYSTEM (NASA) 57 F HC A04/HF A01 CSCI 07D

N77-32242

Unclas

G3/23 47831

NASA TM 73720

**A HIGH PRESSURE MODULATED MOLECULAR BEAM  
MASS SPECTROMETRIC SAMPLING SYSTEM**

by Carl A. Stearns, Fred J. Kohl,  
George C. Fryburg, and Robert A. Miller  
Lewis Research Center  
Cleveland, Ohio 44135  
July 1977



1 Report No <b>NASA TM 73720</b>	2 Government Accession No	3 Recipient's Catalog No	
4 Title and Subtitle <b>A HIGH PRESSURE MODULATED MOLECULAR BEAM MASS SPECTROMETRIC SAMPLING SYSTEM</b>		5 Report Date <b>July 1977</b>	6 Performing Organization Code
		8 Performing Organization Report No <b>E-9270</b>	
7 Author(s) <b>Carl A. Stearns, Fred J. Kohl, George C. Fryburg, and Robert A. Miller</b>		10 Work Unit No	11 Contract or Grant No
9 Performing Organization Name and Address <b>National Aeronautics and Space Administration Lewis Research Center Cleveland, Ohio 44135</b>		13 Type of Report and Period Covered <b>Technical Memorandum</b>	
		14 Sponsoring Agency Code	
12 Sponsoring Agency Name and Address <b>National Aeronautics and Space Administration Washington, D. C. 20546</b>		15 Supplementary Notes	
16 Abstract <p>The current state of understanding of free-jet high pressure sampling is critically reviewed and modifications of certain theoretical and empirical considerations are presented. A high pressure, free-jet expansion, modulated molecular beam, mass spectrometric sampling apparatus was constructed and this apparatus is described in detail. Experimental studies have demonstrated that the apparatus can be used to sample high temperature systems at pressures up to one atmosphere. Condensible high temperature gaseous species have been routinely sampled and the mass spectrometric detector has provided direct identification of sampled species. System sensitivity is better than one tenth of a part per million. Experimental results obtained with argon and nitrogen beams are presented and compared to theoretical predictions. These results and the respective comparisons are taken to indicate acceptable performance of the sampling apparatus. Results are also given for two groups of experiments related to hot corrosion studies. The formation of gaseous sodium sulfate in doped methane-oxygen flames was characterized and the oxidative vaporization of metals was studied in an atmospheric pressure flowing gas system to which gaseous salt partial pressures were added.</p>			
17 Key Words (Suggested by Author(s)) <b>High pressure mass spectrometry; Free jet sampling; Molecular beams; Flame studies; Sodium sulfate</b>		18 Distribution Statement <b>Unclassified - unlimited STAR Category 23</b>	
19 Security Classif. (of this report) <b>Unclassified</b>	20 Security Classif. (of this page) <b>Unclassified</b>	21 No. of Pages	22 Price*

## A HIGH PRESSURE MODULATED MOLECULAR BEAM MASS

### SPECTROMETRIC SAMPLING SYSTEM

by Carl A. Stearns, Fred J. Kohl,  
George C. Fryburg, and Robert A. Miller\*

Lewis Research Center

#### SUMMARY

The current state of understanding of free-jet high pressure sampling is critically reviewed and modifications of certain theoretical and empirical considerations are presented. A high pressure free-jet expansion, modulated molecular beam, mass spectrometric sampling apparatus was constructed and this apparatus is described in detail. Experimental studies have demonstrated that the apparatus can be used to sample high temperature systems at pressures up to one atmosphere. Condensable high temperature gaseous species have been routinely sampled and the mass spectrometric detector has provided direct identification of sampled species. System sensitivity is better than one tenth of a part per million. Experimental results obtained with argon and nitrogen beams are presented and compared to theoretical predictions. These results and the respective comparisons are taken to indicate acceptable performance of the sampling apparatus. Results are also given for two groups of experiments related to hot corrosion studies. The formation of gaseous sodium sulfate in doped methane-oxygen flames was characterized and the oxidative vaporization of metals was studied in an atmospheric pressure flowing gas system to which gaseous salt partial pressures were added.

#### INTRODUCTION

The apparatus described herein was built to facilitate sampling and characterization of gaseous molecular species from various sources at pressures up to one atmosphere. The need for the apparatus derived from our desire to study certain chemical reactions considered fundamental in the hot corrosion process which can occur in gas turbine engines (refs. 1 to 3). Envisioned experiments would involve the sampling of doped flames and flowing gas reaction tube systems. Species to be directly identified and measured would include stable gases, reactive intermediates associated with flames, and low vapor pressure metal-containing high temperature molecules. Therefore, prerequisites for the apparatus were: (1) capability of sampling systems at atmospheric pressure, (2) capacity to sample condensable high temperature gaseous species, (3) mass spectrometric detection to provide direct identification of sampled species and to measure their concentration, (4) sensitivity of parts per million or better, and (5) ability to maintain the chemical and dynamic integrity of the species being sampled.

---

\*National Research Council Resident Research Associate.

Because mass spectrometers are relatively low pressure devices, the apparatus design problem centered on extracting a sample from the high pressure source and transferring it to the mass spectrometer without altering the sample's chemical characteristics in an unpredictable way. Batch and microprobe techniques are precluded for samples containing reactive and condensible species. However, the so-called high pressure free-jet expansion sampling technique appeared to satisfy our prerequisites. In this technique one samples (continuously or intermittently) from high pressure through an orifice into a vacuum to produce a supersonic molecular beam which is compatible with and can be analyzed by a mass spectrometer operating in a low pressure region. This sampling technique has been successfully applied by a number of investigators in quite diverse research areas (refs. 4 to 12 and references cited therein).

Our apparatus was designed in consultation with Drs. F. T. Greene and T. A. Milne of the Midwest Research Institute. The gas sample enters a four stage differentially pumped apparatus through an orifice in the apex of the sampling cone. The gas expands as a free-jet in the first vacuum stage and becomes a supersonic "molecular beam." The central core of the beam is passed by a conical skimmer into the second vacuum stage where the beam is modulated by a rotating segmented disk. After passing through another differential pumping stage the modulated beam enters the fourth very-low pressure vacuum stage and the ion source of a quadrupole mass spectrometer.

Detailed evaluation of the apparatus we constructed established that it satisfied the prerequisites and design criteria. The system has been successfully used to investigate (1) the formation of sodium sulfate in doped flames and flowing gases at atmospheric pressure (ref. 13), and (2) volatile species emanation from metal samples exposed at elevated temperatures to one atmosphere pressure of oxygen containing partial pressures of NaCl(g) and H<sub>2</sub>O(g) (refs. 14 and 15). The sampling apparatus has potential to be applied to a variety of problems where it is desirable to sample systems at pressure up to one atmosphere.

## THEORETICAL ASPECTS OF HIGH PRESSURE SAMPLING

### Beam Formation

When sampling a gas system through an orifice that is not in thermodynamic equilibrium with the source gas, the orifice size should be so selected to insure that the sample represents the bulk source gas and not a stagnant boundary layer near the orifice. For orifice Knudsen numbers,  $Kn_0$ , less than about  $10^{-2}$ , boundary layer effects are insignificant (refs. 16 and 17) and therefore the orifice diameter,  $D_0$ , should be sized to satisfy the criterion  $Kn_0 < 10^{-2}$  for the source gas and conditions of pressure,  $P_0$ , and temperature,  $T_0$ . The orifice Knudsen number is related to the orifice diameter through the mean free path length,  $\lambda_0$ , of the source gas molecules (ref. 18), i.e.,

$$Kn_0 = \frac{\lambda c}{D} \quad (1)$$

When gas flows through an orifice into a lower pressure region, the type of gas flow (effusive, transitional, slip, or continuum) is dictated by the value of  $Kn_0$ . For  $Kn_0 < 10^{-2}$  the source gas expands into the low pressure region by continuum flow (ref. 17). The flow produces a supersonic jet if the pressure ratio across the orifice is greater than about two for most gases (ref. 19). (For most beam systems the pressure ratio is usually made as high as practical,  $>10^4$ , to minimize scattering by background gas in the low pressure region.) The expansion is termed "free-jet" if the orifice has no flow controlling constraints on its downstream side. Because a finite pressure exists in the low pressure region, the supersonic flow field is bounded by a shock system consisting of a barrel shock and a Mach disk or normal shock front. The flow field and shock system are shown schematically in figure 1. The size and shape of the shock system has been studied by Bier and Schmidt (ref. 20 and references cited therein) who showed that these parameters are a function of the pressure ratio across the orifice. Ashkenas and Sherman (ref. 21) have established that the location of the Mach disk is independent of the source gas properties. The location of the Mach disk is given by the equation

$$X_M = 0.67 D_0 \left( \frac{P_0}{P_1} \right)^{1/2} \quad (2)$$

where  $X_M$  is the distance downstream from the orifice to the plane of the Mach disk and  $P_1$  is the pressure in the region downstream of the orifice. Thus we see that the higher the pressure ratio, the further downstream the jet proceeds before being interrupted by the normal shock.

#### Continuum Flow Beam Gas History

The gas history (time or distance-temperature-pressure-density relations) of a free-jet expansion can be approximated as an isentropic expansion where the gas leaves the source as a classical bulk fluid characterized by thermodynamic parameters. In the continuum flow region molecules collide with each other in such a way that the mass flow becomes highly directed and forms a jet. In the flow process the random thermal energy (enthalpy) of the colliding gas molecules is converted to directed kinetic energy and adiabatic cooling of the gas takes place. As the expansion proceeds downstream, the jet density and temperature decrease until a region is reached where collisions become so infrequent that essentially collisionless flow prevails. In this nearly collisionless flow regime a supersonic molecular beam is formed.

A knowledge of the aerodynamics of the supersonic beam is necessary if one expects to estimate the time involved in the beam formation process and the gas history. Extensive research by numerous investigative groups has established an almost complete understanding of the aerodynamics. Excellent reviews and detailed analyses are contained in the literature (refs. 19, 21 to 25 and references cited therein). Our analysis of the beam formation process as presented here is not intended to start with first principles or be all inclusive. Instead we will deal only with those aspects needed to provide a general background for understanding the general principles of the sampling system.

The one-dimensional compressible flow analysis of a perfect gas with complete relaxation (equilibrium), as provided by fluid mechanics (ref. 26), yields the fundamental isentropic expansion equations relating the expanded gas properties to the flow Mach number,  $M$ , and the source gas properties

$$\frac{n}{n_0} = \left[ 1 + \frac{(\gamma - 1)}{2} M^2 \right]^{1/(1-\gamma)} \quad (3)$$

$$\frac{P}{P_0} = \left[ 1 + \frac{(\gamma - 1)}{2} M^2 \right]^{\gamma/(\gamma-1)} \quad (4)$$

$$\frac{T}{T_0} = \left[ 1 + \frac{(\gamma - 1)}{2} M^2 \right]^{-1} \quad (5)$$

$$\frac{n}{n_0} = \frac{P}{P_0}^{1/\gamma} = \left( \frac{T}{T_0} \right)^{1/(\gamma-1)} \quad (6)$$

The density  $n$ , pressure  $P$ , and temperature  $T$  refer to source conditions when subscripted by zero and to expanded gas conditions at  $M$  when not subscripted. The specific heat ratio for the gas is denoted by  $\gamma$ .

For incomplete relaxation, an effective  $\gamma$  may be used.

Mach number is defined as the ratio of the local flow velocity,  $V$ , to the local speed of sound in the fluid,  $c$ , i.e.,

$$M = \frac{V}{c} \quad (7)$$

Ashkenas and Sherman (ref. 21) have derived an expression relating the centerline flow Mach number to the distance  $X$  downstream in the expansion from the orifice. Their expression is

$$M = A \left( \frac{X}{D_C} - \frac{X_0}{D_0} \right)^{\gamma-1} - \frac{\frac{1}{2} \left( \frac{\gamma+1}{\gamma-1} \right)}{A \left( \frac{X}{D_0} - \frac{X_0}{D_0} \right)^{\gamma-1}} \quad (8)$$

where  $A$  and  $(X_0/D_0)$  are constants whose value depends on  $\gamma$  as shown in Table I. From equation (8) it is seen that it is convenient to express distance downstream from the orifice in terms of orifice diameters  $(X/D_0)$ . For distances  $(X/D_0) > 4$ , the centerline Mach number can be approximated by

$$M = A \left( \frac{X}{D_0} \right)^{\gamma-1} \quad (9)$$

for values of  $\gamma = 5/3, 7/5$ , or  $9/7$ . For Mach numbers large in comparison to unity, Knuth (ref. 27) suggests the following equation for all specific heat ratios:

$$M = \left( \frac{2.2}{\sqrt{\gamma(\gamma-1)}} \right)^{\gamma-1/2} \left( \frac{\gamma+1}{\gamma-1} \right)^{\gamma+1/4} \left( \frac{X}{D_0} \right)^{\gamma-1} \quad (10)$$

While Ashkenas and Sherman's expression (eq. (8)) has been shown experimentally to be quite accurate at several orifice diameters downstream (refs. 21 and 28), it has been shown (ref. 28) and is now recognized that this equation does not apply in the transonic region near the orifice. The transonic flow problem is still unsolved but characterization of this flow has been approximated by various sink flow models (refs. 25 and 29), by extrapolation of Ashkenas and Sherman's results (ref. 30), and by empirical expressions derived from experimental measurements (refs. 19 and 31). We have chosen to characterize the flow from the subsonic region upstream of the orifice to the hypersonic region downstream by smoothly extrapolating equation (8) for  $M < 4$  while assuming sonic flow ( $M = 1$ ) at the orifice plane. Although this extrapolation is not based on a physical model, we believe that the results are an adequate approximation for our purposes.

The extrapolation is performed by fitting the Mach number of a third degree polynomial in  $(X/D_0)$ . The polynomial

$$M = a_0 + a_1(X/D_0) + a_2(X/D_0)^2 + a_3(X/D_0)^3 \quad (11)$$

was fit in two ranges of  $(X/D_0)$  by specifying certain conditions for each range. The first range was  $0 \leq (X/D_0) \leq (X/D_0)_{M=4}$  where  $(X/D_0)_{M=4}$  is the distance for  $M = 4$  as calculated by equation (8). In this range the specified conditions were: (1) the flow is choked by the orifice, i.e.,  $M = 1$  at  $(X/D_0) = 0$ ; (2) a point of inflection exists at the orifice, i.e., at  $(X/D_0) = 0$  the second derivative,  $d^2M/d(X/D_0)^2$ , is zero; (3) at  $M = 4$  the polynomial and equation (8) collocate and (4) at  $M = 4$  the polynomial and equation (8) have the same slope. Inspection of the polynomial reveals that condition (1) sets  $a_0 = 1.000$  and condition (2) fixes  $a_2 = 0.000$ .

The second range for fitting the polynomial extended from  $(X/D_0) = 0$  to some distance upstream from the orifice designated  $(X/D_0)_r$  which is the root of the polynomial for the second range. Conditions specified for fitting in this range were: (1) the flow is choked by the orifice, (2) the polynomials for the first and second range collocate at the orifice, (3) the polynomials have equal slopes at the orifice, (4) the second polynomial has an inflection point at the orifice, and (5) at  $(X/D_0)_r$  the slope is zero.

For all conditions specified, the following general polynomials result for the two ranges

$$\text{Range 1:} \quad M = 1 + a_1(X/D_0) + a_3(X/D_0)^3 \quad (12)$$

$$\text{Range 2:} \quad M = 1 + a_1(X/D_0) - \frac{4}{27} a_1^3 (X/D_0)^3 \quad (13)$$

The root of the second polynomial is  $(X/D_0)_r = -\frac{3}{2a_1}$ , and the polynomials obtained for  $\gamma = 5/3, 7/5, \text{ and } 9/7$  are presented in Table II. The polynomials and equation (8) were used to calculate the Mach number against distance plots shown in figure 2. These curves show, as we initially assumed, that the gas expansion actually begins slightly upstream of the orifice and this is in substantial agreement with experimental measurements and results obtained by other approximations.

The results presented in figure 2 provide a characterization of the aerodynamics of the free-jet expansion which can be used to estimate the gas history. The hydrodynamic flow velocity is given by

$$V = Mc = D_0 \frac{d(X/D_0)}{dt} \quad (14)$$

and the speed of sound is a function of the local gas temperature,  $T$ , and molecular weight,  $M$  (ref. 18),

$$c = \left( \frac{\gamma RT}{M} \right)^{1/2} \quad (15)$$

where  $R$  is the gas constant ( $8.3143 \text{ J K}^{-1} \text{ mol}^{-1}$  or  $8.3143 \times 10^7 \text{ erg K}^{-1} \text{ mol}^{-1}$ ). For the isentropic expansion the local gas temperature of the jet can be expressed in terms of the source gas temperature (by eq (5)) giving

$$c = \left( \frac{\gamma R}{M} \right)^{1/2} T_0^{1/2} \left[ 1 + \frac{(\gamma - 1)}{2} M^2 \right]^{-1/2} \quad (16)$$

or

$$c = c_0 \left[ 1 + \frac{(\gamma - 1)}{2} M^2 \right]^{-1/2} \quad (17)$$

where  $c_0$  is the speed of sound in the source gas. From equations (14) and (17) it follows that

$$\frac{c_0}{D_0} dt = \left[ \frac{1}{M^2} + \frac{(\gamma - 1)}{2} \right]^{1/2} d(X/D_0) \quad (18)$$

Integration of this equation yields the time-distance profile for the expanding gas. The profiles obtained by numerical integration of equation (18) for the specific heat ratios 5/3, 7/5, and 9/7 are shown in figure 3. In this figure time is plotted as the dimensionless flow time parameter  $c_0 t/D_0$  and distance is scaled in terms of orifice diameters.

Combining the data of figures 2 and 3 with the appropriate isentropic expansion relations (eqs. (3) to (6)) allows one to determine the temperature, density, or pressure at any point or time in the expansion. These various relations are shown graphically in figures 4 and 5 where the parameters ratioed to source conditions are plotted against time and distance, respectively. While these figures clearly indicate the rapidity of the expansion, a more tangible appreciation of the time involved can be obtained by considering an actual gas on a real time basis. The expansion history of argon source gas expanding through a 0.025 centimeter diameter orifice is shown in figure 6. Here we see that major reductions in temperature, density, and pressure take place in only a few microseconds. This feature of the free-jet expansion accounts for the applicability of this technique to sampling (refs. 29 and 32).

#### Beam Gas History Beyond Continuum Flow Region

From the preceding discussion one might intuitively presume that at sufficiently large distances from the jet source the density becomes so low that there are essentially no collisions. Theoretical and experimental studies have shown that there is a limiting region in the flow field beyond which further cooling and acceleration are precluded by the rarefied nature of the flow (ref. 19). Thus there is a transition from the collision dominated continuum flow to a nearly collisionless molecular flow regime. Extensive effort has been directed to understanding the transition flow regime and as pointed out by Anderson (ref. 19) there is a hierarchy of theories. This hierarchy is based on the degree of accuracy and detail provided by the theories. The direct simulation Monte Carlo method as applied by Bird (ref. 33) has provided an almost complete understanding of the transition flow regime but a detailed analysis of this regime is beyond the scope of our presentation. For our purposes it is only necessary to comprehend certain aspects of transition flow. To this end we will consider a simplified treatment which has proven to be adequate for predicting some jet properties

Anderson and Fenn (ref. 34) measured velocity distributions of molecular beams extracted from free jets. They found that the transition to free molecular flow could for convenience be compared to phenomenon occurring in effusive flow. For effusive flow the velocity distribution in the axial direction does not change with increasing distance from the molecular beam source. The axial (parallel) molecular velocity distribution is thus said to be "frozen in." Conversely, the radial (perpendicular) distribution approaches zero with increasing distance from the source. (This is a consequence of the fact that the molecules travel in straight line paths and there are no collisions.) For the effusive source the distribution of velocities is anisotropic with a wide distribution in the parallel direction and a narrow distribution in the perpendicular direction.

For continuum flow the distribution of velocities is isotropic with equal parallel and perpendicular distributions. No freezing of the parallel distribution takes place in continuum flow and the velocity spread of the distribution decreases with increasing distance from the jet source.

In considering expanding source flow it is useful to define a parallel temperature,  $T_{||}$ , and a perpendicular temperature,  $T_{\perp}$ . These are the temperatures of a two-dimensional Maxwellian distribution function which describes the local distribution of molecular speeds in the radial direction and in a direction perpendicular to the radial direction. For continuum flow where the speed distribution is isotropic,  $T_{\perp} = T_{||}$ . The transition flow problem then can be considered as one of determining how  $T_{||}$  and  $T_{\perp}$  vary in the expansion as the transition regime is passed through.

#### Terminal Mach Number

In the "free molecular flow" region of a free-jet expansion Anderson and Fenn (ref. 34) showed that a freezing of the parallel distribution occurred. They found nonisotropic distributions where the perpendicular direction had a narrower distribution width than that of the parallel direction. Their model of the transition regime yielded an expression for a terminal Mach number,  $M_T$ , that was in substantial agreement with their experimental observations and those from other laboratories. The terminal Mach number expression was derived by considering the point in the expansion beyond which the temperature cannot change as rapidly as required for isentropic continuum behavior. The Mach number at this point,  $M_1$ , represents the value where collision domination of the jet flow ceases. The terminal Mach number then represents the asymptotic value which the Mach number approaches at infinite distances downstream from the source. Anderson and Fenn's terminal Mach number can be expressed in the generalized form

$$M_T = \left( \frac{\gamma}{\gamma - 1} \right) \left( \frac{2}{A} \right)^{1/\gamma} \left( \frac{8}{\gamma\pi} \right)^{(\gamma-1)/2\gamma} \left( \frac{Kn_c}{t} \right)^{(1-\gamma)/\gamma} \quad (19)$$

where  $A$  is the constant in Ashkenas and Sherman's Mach number expression

(eq. (8)) and  $\epsilon^*$  is the collision effectiveness. For  $\gamma = 5/3, 7/5, \text{ and } 9/7$ , the respective terminal Mach numbers reduce to

$$M_{T(\gamma=5/3)} = 2.03 \left( \frac{Kn_0}{\epsilon} \right)^{-0.400} \quad (20)$$

$$M_{T(\gamma=7/5)} = 2.48 \left( \frac{Kn_0}{\epsilon} \right)^{-0.286} \quad (21)$$

$$M_{T(\gamma=9/7)} = 2.85 \left( \frac{Kn_0}{\epsilon} \right)^{-0.222} \quad (22)$$

Anderson and Fenn's experimental data for  $\gamma = 5/3$  yielded a value for the collision effectiveness of  $\epsilon = 0.25$ . Their equation for  $M_T$  can be expressed in the generalized form

$$M_T = \frac{M_T}{\gamma} \quad (23)$$

and the distance from the source orifice to where  $M_T$  is reached can be calculated from equation (8).

### Beam Intensity

Thus far in our analysis of the beam formation process no consideration has been given to the question of beam intensity. From a practical point of view, intensity is a key parameter if free-jet expansion techniques are to be used in sampling. With a conventional effusive or oven beam source, the maximum attainable intensity in the collimated molecular beam is limited by two factors for any given oven temperature. These factors are: (1) the effusion through the orifice and (2) geometrical factors involved in obtaining a collimated beam from the random initial velocities of the effusing molecules. Kantrowitz and Grey (ref. 35) suggested that these limitations could be overcome by placing a collimating element in the flow from a sonic nozzle. Their analysis indicated that the mass motion from a sonic orifice provides an initial collimation which improves the flow rate and geometrical factors so that a net beam intensification results. Their work provided much of the impetus for development of the free-jet expansion sampling technique.

#### (a) Continuum Flow at the Skimmer

The Kantrowitz and Grey analysis is based on four critical assumptions: (1) the continuum flow field extends to the first collimating element (hereafter called the skimmer); (2) the continuum flow is isentropic;

(3) the flow at the skimmer is parallel and undisturbed by the presence of the skimmer; and, (4) the flow downstream from the skimmer is collisionless. On the basis of these assumptions, and by neglecting the component of the random molecular thermal velocity in the direction of the mass flow. Kantrowitz and Grey derived expressions for the velocity distribution and "precollimation gain" in beam intensity. Parker et al. (ref. 36) made a similar analysis without making the mathematical simplification of neglecting the random thermal velocity component parallel to the beam. For Mach numbers greater than three the results of both analyses are essentially the same.

The axial differential number density can be expressed as

$$\frac{dn(u)}{du} \propto u^2 \exp \left[ -\left(\frac{u - V}{\alpha}\right)^2 \right] \quad (24)$$

where  $u$  is the molecular velocity,  $V$  is the flow velocity, and  $\alpha$  is the most probable thermal velocity at the translational temperature  $T$  which is given by the isentropic flow relation (eq. (5)). The most probable velocity of the supersonic molecular beam,  $u_{mp}$ , is obtained by determining the maximum for the distribution given by equation (24),

$$u_{mp} = \frac{1}{2} \left[ V + (V^2 + 4\alpha^2)^{1/2} \right] \quad (25)$$

Thus it is apparent that for the supersonic beam the distribution is narrower than the Maxwellian distribution for an effusive beam where  $M = 0$  and  $V = 0$ . Also, the supersonic distribution is seen to move to higher velocities and become narrower as  $M$  increases. At the limit of infinite Mach number the distribution is monoenergetic with velocity  $V$ .

The theoretical equation for the centerline flux at a detector, located a distance  $l$  downstream from the skimmer, derived by Parker et al. is given by

$$J_d = \frac{n_s A_s c_0}{4\pi l^2} \left[ \frac{M_s (3 + \gamma M_s^2) (1 + \operatorname{erf} \sqrt{\gamma M_s^2 / 2}) + \sqrt{2/\gamma} (2 + \gamma M_s^2) \exp\left(-\frac{\gamma M_s^2}{2}\right)}{[1 + (\gamma - 1)M_s^2 / 2]^{1/2}} \right] \quad (26)$$

where  $n_s$  is the density at the skimmer,  $A_s$  is the area of the skimmer orifice, and  $M_s$  is the Mach number at the skimmer. This equation is based on the four idealization assumptions of Kantrowitz and Grey. For  $M_s > 3$ , the centerline flux at the detector can be approximated by

$$J_d = \frac{n_s A_s c_0}{2\pi l^2} \left\{ \frac{M_s (\gamma M_s^2 + 3)}{[1 + (\gamma - 1)M_s^2 / 2]^{1/2}} \right\} \quad (27)$$

or

$$J_d = \frac{n_s A_s V_s}{2\pi\ell^2} (\gamma M_s^2 + 3) \quad (28)$$

where  $V_s$  is the flow velocity at the skimmer.

Because the mass spectrometer detector used in our apparatus is a density sensitive device, we are concerned with detector signals which are proportional to number density. In terms of number density at the detector,  $n_d$ , equation (28) can be expressed as

$$n_d = \frac{n_s A_s}{2\pi\ell^2} (\gamma M_s^2 + 3) \quad (29)$$

Knuth (ref. 25) and Anderson et al. (ref. 34) recognized that beam divergence would effect beam intensity at the detector and derived equations to account for divergence. Their analysis again assumes continuum flow to the skimmer and collisionless flow downstream from the skimmer. For the usually encountered experimental case where the orifice to skimmer distance,  $X_s$ , is much smaller than the skimmer to detector distance,  $\ell$ , Knuth derives the distribution

$$\frac{dn_d}{du} = \frac{2}{\sqrt{\pi}} \left(\frac{X_s}{\ell}\right)^2 n_s \cos \beta \sin \beta d\beta \frac{u^2}{\alpha^3} \exp\left\{-\left[\frac{u^2}{c^2} - \frac{2u}{\alpha} \cos \beta + S_s^2\right]\right\} \quad (30)$$

where  $S_s = M_s \sqrt{\gamma/2}$  and  $\beta$  is the half angle subtended by the skimmer at the source as shown in figure 7. When equation (30) is integrated over all velocities,  $u = 0$  to  $u = \infty$ , and over  $\beta$  from 0 to  $\beta$ , a general equation for the number density at the detector results

$$n_d = \left[ \frac{n_s}{4} \left(\frac{X_s}{\ell}\right)^2 \frac{1}{S_s^2} \right] \left[ \left(1 - 2S_s^2 \cos^2 \beta\right) (1 + \operatorname{erf} S_s \cos \beta) \exp(-S_s^2 \sin^2 \beta) \right. \\ \left. + \frac{2}{\sqrt{\pi}} (1 - \cos \beta) S_s \exp(-S_s^2) + (2S_s^2 - 1)(1 + \operatorname{erf} S_s) \right] \quad (31)$$

For small skimmer openings and high Mach numbers at the skimmer, i.e.,  $\cos \beta \approx 1$ ,  $S_s \cos \beta \gg 1$  and  $2S_s^2 \gg 1$ , equation (31) can be reduced to the more tractable approximate form

$$n_d = n_s \left(\frac{X_s}{\ell}\right)^2 \left[ 1 - \cos^2 \beta \exp(-S_s^2 \sin^2 \beta) \right] \quad (32)$$

If parallel flow to the skimmer is assumed (i.e., if divergence is neglected) so that  $\sin \beta = \beta$  and  $\cos \beta = 1$ , equation (30) can be integrated to give

$$n_d = \frac{n_s A_s}{2l^2 \pi^{3/2}} \left[ \sqrt{\pi} \left( S_s^2 + \frac{1}{2} \right) (1 + \operatorname{erf} S_s) + S_s \exp(-S_s^2) \right] \quad (33)$$

Equations similar to (32) and (33) have been derived by LeRoy and Govers (ref. 37), Hagena and Morton (ref. 38), Anderson (ref. 19), and French (ref. 39). The above equations can be used to calculate an "idealized" theoretical density at the detector for the case where the skimmer is placed close enough to the source orifice to be in the continuum flow field. In practice however, this case is usually avoided for high pressure sampling systems. Generally the skimmer is positioned relatively far from the orifice to provide adequate pumping in this region and to reduce skimmer interference. (Usually the experimenter measures intensity as a function of  $X_s$  to find where the experimental maximum occurs.) Experimental considerations thus dictate the necessity for having skimmer to orifice distances sufficiently large to preclude continuum flow to the skimmer. Therefore we must now examine the case where the transition from continuum flow takes place upstream of the skimmer.

#### (b) Transition Flow Upstream of the Skimmer

Downstream from the onset of translational freezing a relatively broad velocity distribution is found in the radial direction, and this greatly influences the axial beam intensity at the detector. Experimental determinations of  $T_{\perp}$  show a dependence on orifice to skimmer distance which is intermediate between the collision dominated form

$$\left( T_{\perp} = T_{\parallel} \propto X_s^{-4/3} \right) \text{ and that expected in the free molecular limit } \left( T_{\perp} \propto X_s^{-2} \right).$$

The variation of  $T_{\perp}$  with downstream distance from the orifice has been attributed to the removal of collision partners from the beam core caused by the relatively large transverse velocities imparted by collisions after the onset of translational freezing (ref. 40).

Hamel and Willis (ref. 41) presented a physical explanation of the situation which is useful to follow. As the gas expands  $T_{\perp}$  decreases due to the geometrical effect of the source flow spherical expansion but in the collision dominated range energy is transferred between the parallel and perpendicular modes of motion because  $T_{\parallel} > T_{\perp}$ . The collisional drain of energy cools  $T_{\parallel}$  so in the collision dominated limit  $T_{\parallel} = T_{\perp}$  and these temperatures vary in proportion to the reciprocal of the distance from the orifice to the 4/3 power. As collisions become less frequent  $T_{\perp}$  still decreases due to geometric expansion but collisional cooling of  $T_{\parallel}$  decreases and eventually freezes. A relatively small collisional transfer of energy still takes place after translational freezing occurs but because  $T_{\parallel} \gg T_{\perp}$  this has a small effect on  $T_{\parallel}$  but a discernible effect

on the perpendicular temperature and  $T_{\perp}$  does not decay as expected in the free molecular case. Thus collisions are more effective in the rarefied regime in inhibiting the decay of  $T_{\perp}$ . Therefore,  $T_{\perp}$  does not decrease as the reciprocal of distance squared as expected in the free molecular limit.

From the preceding discussion we can see that the beam core does not become collisionless and this effects the intensity at the detector. Sharma et al. (ref. 42) and LeRoy et al. (ref. 40) give the expression for the density at the detector as

$$n_d = n_s \left( \frac{X_s}{l} \right)^2 \left[ 1 - \exp\left(-S_{\perp s}^2 \beta^2\right) \right] \quad (34)$$

where  $S_{\perp s}$  is the perpendicular speed ratio at the skimmer, i.e., the flow speed divided by the most probable random speed perpendicular to the flow velocity at the skimmer. In the derivation of equation (34) it was assumed that  $X_s \ll l$ ,  $\sin \beta = \beta$  and  $\cos \beta = 1$ . Remembering that  $S = M\sqrt{\gamma/2}$  and approximating  $\beta = r_s/X_s$ , where  $r_s$  is the radius of the skimmer opening, equation (34) can be written as

$$n_d = n_s \left( \frac{X_s}{l} \right)^2 \left[ 1 - \exp\left(-M_{\perp s}^2 \frac{\gamma}{2} \frac{r_s^2}{X_s^2}\right) \right] \quad (35)$$

We shall use this equation to calculate idealized theoretical densities because it is relatively easy to apply and because the comparisons made by LeRoy and Govers (ref. 37) indicate that it is a reasonable approximation for our purposes.

When using equation (35) we use two different methods of determining  $M_{\perp s}$ . The first method is based on a sudden freeze approximation while the second method is based on expressions derived by Sharma et al. (ref. 42) from correlations with experimental data. The first method, when applied to our experimental conditions, yields theoretical densities which are about three times greater than our experimentally measured densities. However, the second method predicts theoretical densities which are in good agreement with our experimental measurements.

#### (1) Sudden Freeze Approximation for $M_{\perp s}$

For this method the expansion is assumed to be isentropic to some distance,  $X_q$ , downstream from the orifice. When the orifice to skimmer distance,  $X_s$ , is greater than  $X_q$ , the Mach number at  $X_q$  is taken as the terminal Mach number, i.e.,  $M_T = M_q$ , and

$$M_q = A \left( \frac{X_q}{D_0} \right)^{\gamma-1} \quad (36)$$

This use of  $M_T$  is equivalent to assuming continuum flow upstream of  $X_q$  and molecular flow downstream from this point. With this assumption it follows that  $T_1/T_q = (X_q/X_s)^2$ , where  $T_q$  is the translational temperature at  $M_q$  calculated from isentropic relations, and

$$M_{1s} = M_q \left( \frac{X_s}{X_q} \right) \quad (37)$$

At  $X_q$  the density  $n_q$  is calculated from

$$n_q = n_0 \left[ 1 + \frac{(\gamma-1)}{2} M_q^2 \right]^{1/1-\gamma} \quad (38)$$

and the density at the skimmer is assumed to decrease according to

$$n_s = n_q \left( \frac{X_q}{X_s} \right)^2 \quad (39)$$

Therefore, the idealized density at the detector can be calculated for a given system geometry and source gas conditions, i.e., given  $X_s$ ,  $l$ ,  $D_0$ ,  $r_s$ ,  $\gamma$ ,  $n_0$ ,  $P_0$ , and  $T_0$ .

## (2) Experimental Correlations for $M_{1s}$

Sharma et al. (ref. 42) correlate experimental results for monatomic gases to obtain equations for calculating  $M_{1s}$ . The data on perpendicular temperatures indicate that this temperature decreases as though the expansion were isentropic to a transition point located several times as far from the source as is the point at which  $T_{1s}$  begins to deviate for an isentropic expansion. The distance downstream from the source orifice to this transition point is given by

$$\frac{x_{11}}{D_0} = 4.58 \left( \frac{D_0}{\tau_0 c_0} \right)^{0.6} \quad (40)$$

where  $\tau_0$  is the characteristic time for translational relaxation of the gas species as given by

$$\tau_0 = \frac{15}{8} \left( \frac{1}{\sqrt{2} n_0 \sigma^2} \right) \left( \frac{\pi M}{8RT_0} \right)^{1/2} \quad (41)$$

Here  $\sigma$  is the collision diameter and  $M$  is the molecular weight of the source gas at temperature  $T_0$  and with density  $n_0$ . From the argon jet data of Habets et al. (ref. 43), who found  $S_1 = X/R$  (where  $R$  is a function of source conditions), Sharma et al. develop the expression

$$M_{1s} = \frac{2.50}{\sqrt{\gamma}} \left( \frac{D_0}{\tau_0 c_0} \right)^{-0.2} \left( \frac{X_s}{D_0} \right) \quad (42)$$

For the second method calculations equation (42) is used to obtain the value of  $M_{1s}$  used in equation (35) and  $n_s$  is calculated exactly the same as for method one.

#### APPARATUS

Our high pressure mass spectrometric sampling apparatus is shown in figure 8. Before proceeding with a detailed description it is instructive to consider the entire system briefly in general terms.

A schematic cross-sectional view of the beam path portion of the sampler is shown in figure 9. The atmospheric pressure gas to be sampled enters the system through the sampling orifice located at the bottom of the vertical configuration. For sampling orifice Knudsen number less than  $10^{-2}$  the gas expands into stage I as a free jet. Stage I vacuum pumping maintains pressure ratios greater than  $10^5$  across the sampling orifice. The conical skimmer intercepts the gas flow and passes the central portion or core of the flow into stage II where the core is periodically interrupted by a toothed rotating disk beam chopper. Pressure in stage II is less than  $10^{-5}$  torr. The chopped gas beam enters the stage III differential pumping vacuum chamber through a collimating aperture. Pressure in stage III is less than  $10^{-6}$  torr. The beam exits from stage III through another aperture and passes into stage IV and the ionizer of the quadrupole mass spectrometer. Pressure in stage IV is less than  $10^{-7}$  torr. Ions formed in the electron bombardment ionizer are electrically focused and transmitted to the quadrupole mass filter. Selected ions transmitted by the filter are electrically deflected into the off-axis electron multiplier whose output is electronically monitored. Thus a gas sample at high pressure is continuously transferred to the low pressure mass spectrometer where the gas is analyzed on the basis of the mass-to-charge ratio of its constituents. Maintaining the fidelity of the sample depends on specific design parameters of the apparatus. These parameters will be considered in detail for the various components of the apparatus.

#### Vacuum Systems

Plan views of the stages I through IV vacuum chambers are shown in figure 10 where the letters designate flanged ports. This portion of the

apparatus was designed in consultation with Drs. F. T. Greene and T. A. Milne of the Midwest Research Institute. The vacuum chambers, skimmer, beam collimator, and chopper assembly were constructed under contract by the Midwest Research Institute.

All vacuum chambers are constructed of stainless steel, mechanical pump lines are copper, O-rings are Viton, ionization gage tubes are Bayard-Alpert type and diffusion pump fluid is Santovac 5. The vacuum system for each stage is controlled by a manual/automatic electrical control system. In the automatic mode of operation an ionization gage is the primary element controlling a pneumatic high vacuum valve which isolates the vacuum chamber from the respective diffusion pump. A thermocouple gage tube, located at the diffusion pump exhaust, controls the diffusion pump power and a pneumatic valve in the fore line. Diffusion pump temperature and water flow interlocks are also part of the electrical control system.

The overall size of the vacuum system was made to make the beam path as short as possible while providing sufficient pumping speed for each stage. The stage I pumping requirements were most critical and thus this stage set the general scale of the apparatus. The size of the stage I vacuum chamber was dictated by conductance requirements and physical considerations related to pump size and location. Stage I is pumped by two liquid nitrogen trapped 10-inch diffusion pumps. Each trap-pump combination is attached to the stage I chamber, with O-ring seals, at flanges G. Nominal conductance for each cold trap is 4200 liters per second and the maximum air pumping speed of each diffusion pump is 5300 liters per second. Each diffusion pump is backed by a direct drive two-stage rotary mechanical vacuum pump with a maximum pumping speed of 61 liters per second. These mechanical pumps are also used to rough pump stage I through 4-inch lines connected to the chamber by way of manually operated slide valves attached to flanges B. The cold trap-diffusion pump can be isolated from the chamber, approximately at flange G, by specially designed air operated lift valves. These valves' pneumatic operators are attached at flanges C. Stage I pressure is measured with either the ionization gage tube connected to flange A, or a capacitance type gage located at flange A<sub>4</sub>. The capacitance gage has a range to one torr full scale and a resolution of one part in 10<sup>5</sup>. Flange E accepts the sampling orifice inlet assembly which will be described later.

The stage II vacuum chamber is the rectangular parallelepiped located in the top-center section of the stage I chamber. The stage II chamber is evacuated through a 6-inch diameter pipe which physically passes through the stage I chamber, but is isolated from it for vacuum purposes. This pipe terminates at flange F. A 6-inch diffusion pump-liquid nitrogen cold trap combination is connected to flange F through a 6 inch, pneumatically operated, slide valve. Conductance of the trap is 1700 liters per second and the maximum air pumping speed of the diffusion pump is 2400 liters per second. An 8.5 liters per second two-stage rotary mechanical pump is used to back the diffusion pump and rough pump stage II

through appropriate valving attached to flange  $A_2$ . Pressure in stage II is measured with an ionization gage tube connected to flange  $A_3$ . The stage I and II vacuum chambers are interconnected through the skimmer assembly which is mounted on the internal flange S shown in figure 9.

The stage III vacuum chamber consists of a vertical cylindrical section and horizontal length of pipe extending to the rear and terminating at flange I. The circular cross section of the pipe is compressed into an elliptical section where it is welded to the vertical cylinder. Stages III and II are interconnected through the collimator assembly mounted on the internal flange T shown in figure 9. A 4-inch diffusion pump-liquid nitrogen cold trap combination is used to evacuate stage III. These are attached at flange I through an elbow and pneumatically operated slide valve. Nominal conductance of the trap is 275 liters per second and the maximum air pumping speed of the diffusion pump is 700 liters per second. An 8.5 liters per second two-stage rotary mechanical pump is used to back the diffusion and rough pump stage III through a pipe appropriately valved and connected to the elbow above the slide valve. Pressures in this stage are measured with an ionization gage tube connected to flange  $A_5$ .

The stage III vacuum chamber can be isolated from stage IV by a specially designed valve. This bellows sealed, manually operated valve is located in stage III. Valve opening and closing are accomplished by translating a ball mechanism. In the open position the ball is retracted to provide a clear passage from stage III to stage IV. In the closed position the ball seats on an O-ring installed around a 0.32 centimeter diameter opening in flange H. The valve mechanism is operated through a bellows attached to flange V.

The cylindrical tee-section attached to flange H comprises the stage IV vacuum chamber. This chamber houses the quadrupole mass spectrometer. All vacuum connections to stage IV are made with copper gasket seals. A 1000 liters per second (air) baffled getter-ion pump, attached to flange J through an elbow, is used to evacuate stage IV. The mass spectrometer is mounted on a flange which mates with flange K. Pressure is measured with an ionization gage tube connected to flange  $A_6$ .

#### Sampling Orifice Inlet Assembly

The three assemblies shown in figure 11 have been used for various experiments. Flange L, which mates directly with flange E of the stage I vacuum chamber, and spacer ring LS is common to each assembly with either flange  $M_1$ ,  $M_2$ , or  $M_3$ . Spacer rings of various height are used to give the desired orifice to skimmer distance. Four screws pass radially, 90 degrees apart, through flange L as shown in figure 11. These screws facilitate lateral movement of the orifice flange, M, for alinement purposes.

Flanges  $M_1$  or  $M_3$  are used when it is desired to allow the sampling orifice to get hot, and flange  $M_2$  is used when a cooled orifice is desired. In the  $M_1$  configuration the platinum orifice cone is welded directly to

the stainless steel plate. Here a type I orifice is used and its geometry is given in figure 12. For the  $M_2$  configuration a type II orifice is soldered directly to the water cooled plate. The  $M_3$  configuration uses a type II orifice welded to the end of the stainless steel tube extension attached to the stainless steel plate. In configurations  $M_1$  and  $M_3$  the stainless steel plate is attached to a water cooled plate and vacuum seal is made with an O-ring. The water cooling in these configurations is used only to protect the O-rings.

With the two types of platinum-rhodium alloy sampling cones shown in figure 12, the orifice is located in the apex of the cone. The orifice is machined so as to produce a sharp edged circular opening with zero channel length.

#### Vertically Translatable Orifice Inlet Assembly

For experiments where it was necessary to have a continuously variable orifice-to-skimmer spacing and reduced source gas pressures, the special assembly shown schematically in figure 13 was used. This unit was added to the apparatus by substituting it for flange M of figure 11. By turning the screw collar the orifice to skimmer distance could be continuously varied with a precision of better than 0.02 centimeter. The cylindrical source chamber is keyed to the housing so that the chamber and orifice do not rotate during vertical translation.

Pressure in the source chamber could be varied from a few microns to 800 torr by suitable vacuum pumping and pressurization from gas cylinders. A mechanical pump was used for evacuation of this chamber. Pressures below 1 torr were measured with a capacitance type vacuum gage. For source chamber pressures above 1 torr a precision dial type gage was used to measure pressure.

When sampling from the source chamber, the gas under investigation was continuously admitted to the chamber through leak valves and the flow rate was adjusted to maintain the desired pressure in the source chamber. A type II sampling cone was soldered to the upper end of the source chamber and the orifice diameter was 0.025 centimeter. The general design of this unit provided good stage I pumping in the vicinity of the orifice even at small orifice-to-skimmer distances.

#### Skimmer and Collimator Assemblies

Cross sectional schematic views of the skimmer and collimator are shown in figures 14 and 15, respectively. The flange mounting portion of these assemblies are similar and they will be described together. The skimmer and collimator flanges mate with an intermediate flange as shown in figure 14. The intermediate flanges in turn mate with flange S (fig. 9) for the skimmer and flange T (fig. 9) for the collimator. The intermediate

flange in each case is located with dowel pins to the flanges S or T. A screw retaining ring serves as a clamp. When the retaining screws are secured in place and the lockdown screws are removed, the assembly can be removed from the apparatus. The assembly can then be replaced in the apparatus, using the dowel locating pins, in exactly the same place as before removal. With both the retaining and lockdown screws in place but not tightened, the skimmer or collimator can be moved laterally for alignment purposes. Once alignment is achieved, securing the retaining screws fixes the position of the skimmer or collimator, respectively.

The skimmer cone is spun from 0.025 inch thick copper. The opening in the apex of the 60 degree cone is machined in a way to provide a sharp edged circular opening with zero channel length. For all the experiments reported here a single skimmer was employed and it had a 0.076 centimeter diameter opening.

The collimator cone is made similarly to the skimmer but with an included angle of 120 degrees and a 0.159 centimeter diameter opening.

#### Beam Chopper Assembly

The beam chopper assembly consists of a motor driven segmented disc, a light bulb and a photo diode detector. This assembly is located in the stage II vacuum chamber and attached to the collimator as shown schematically in figure 16. The rotating disc is made of 0.032 inch thick aluminum. The disc is shaped as shown in figure 17 and carefully balanced to yield vibration free rotation.

A chopping frequency of 150 hertz was routinely employed in our studies. The motor rotation speed was electrically adjusted to produce the desired frequency as measured with the lamp-diode combination. Electrical connections to the beam chopper were made through an insulated feed through attached to flange A7 shown in figure 10.

#### Quadrupole Mass Spectrometer

An Extranuclear Laboratories Inc. quadrupole mass spectrometer system is used in our apparatus. This system is composed of the following model number components: 041-1 axial ionizer, 021-1 electron energy-emission control, 4-270-9 ELFS quadrupole mass filter with  $1.6 \times 22.0$  cm poles, 011-15 power supply - 1 to 6 MHz, 1.25 MHz high-Q head, 031-3 electrometer, 032-5 preamplifier, channeltron electron multiplier and 091-6 digital mass programmer. The quadrupole mass filter has a nominal range from 0 to 500 AMU but in practice we have been able to operate above 600 AMU.

The entire spectrometer is mounted on an 8-inch diameter copper gasket type flange which mates directly to flange K of the stage IV vacuum chamber. All electrical connections to the spectrometer are brought out through

its mounting flange. This flange is also equipped with a window to provide a clear line of sight through the entire spectrometer. An electrically operated shutter protects the window from condensable species in the beam.

Entrance into the mass spectrometer electron bombardment ionizer is through a 0.32 centimeter diameter aperture. The mass spectrometer is physically positioned in the stage IV vacuum chamber to locate the entrance aperture approximately 1 centimeter above the stage III exit aperture. Three bellows sealed micrometer screws are located at the lower end of the stage IV chamber 120 degrees apart radially. These screws bear against the quadrupole mass filter pole housing and facilitate centering the entrance aperture with respect to the stage III exit opening. This positioning can be accomplished while stage IV is under high vacuum.

#### Signal Processing

Beam modulation and phase sensitive detection techniques are used in signal processing to increase the signal-to-noise ratio, S/N. The signal of interest is the ion current produced by ionization of the chopped sample gas beam. There are numerous sources of noise signal and one of these is the signal due to background gas which finds its way into the ionizer.

Beam modulation is achieved with the chopper assembly which both periodically interrupts the gas beam and produces a square wave reference voltage at the modulation frequency. A schematic wiring diagram of the chopper system is shown in figure 18. The variable frequency oscillator output is adjusted in frequency and amplitude to make the motor speed of rotation appropriate to result in the desired chopping frequency. A regulated fixed current is passed through the lamp and as the sectored disk allows light to illuminate the photo diode, an output reference signal voltage is produced. This square wave reference signal at the modulation frequency is used to drive the synchronous gate in the phase sensitive detector signal processor. A Princeton Applied Research model HR-8 lock-in amplifier is the signal processor.

The output of the spectrometer electron multiplier is fed directly into the 032-5 preamplifier mounted in close proximity to the signal feed through in the spectrometer support flange. The preamplifier contains remotely selectable input resistors of  $10^5$ ,  $10^7$ , and  $10^8$  ohms. The output of the preamplifier is routed in parallel to the electrometer, the lock-in amplifier, an oscilloscope, and the digital mass programmer. Signal routing is shown in figure 19.

The d.c. output of the electrometer is proportional to the total ion current, i.e., the sum of (1) the average value of the ion current produced from the chopped gas beam, (2) the ion current resulting from background gas which enters the ionizer, and (3) noise current. The electrom-

eter output can be filtered with preselectable time constants to smooth the signal.

The d.c. output of the lock-in amplifier is proportional to the component of the total ion current that is in phase with the modulated gas beam pulses. Of course the lock-in amplifier must be appropriately tuned with regard to synchronization frequency and phase angle. The lock-in amplifier output can also be filtered with preselectable time constants.

Electrometer and lock-in amplifier outputs are recorded on separate channels of a two channel high speed servo recorder.

The quadrupole mass filter is controlled by a power supply which provides three options for making the filter sweep through an AMU range. In the manual mode, the operator manually adjusts the control potentiometer to sweep the mass filter. A fixed setting of this potentiometer corresponds to a fixed AMU position for the filter and thus one can tune the filter to rest on any AMU of interest. In the sweep mode the filter sweep rate follows the saw tooth ramp rate selected for the oscilloscope. In this mode the AMU starting point and range are independently selectable by the operator. The third sweep mode is labeled external command. In this mode the sweep rate, starting AMU, and AMU range are controlled by commands received from the 091-6 mass programmer. The operator digitally programs the mass programmer; there are sixteen channels which can be programmed. A single channel can be made controlling or all sixteen channels can be run through sequentially.

The mass programmer also contains a signal processing section where the ion current signal can be amplified by a factor from 0.01 to 99.9 according to programmable command for each of the sixteen channels. This has proven to be a useful feature which we alternately employ by suitable switching as shown in figure 19.

## PROCEDURE

### Alignment

Optimum performance of the sampling system is critically dependent upon proper alignment of all orifices and apertures in the gas beam path. A low power (0.2 mW) helium-neon laser is used to align our system. The laser is supported by a mechanism which facilitates setting the beam vertically and translating the beam in two directions perpendicular to the vertical. The exit opening from stage III is fixed in position on the apparatus and therefore all alignment is done relative to this element. The laser is pointed up through the system from the bottom and the beam is centered in the stage III exit opening with all other elements removed from the apparatus. Next the quadrupole mass spectrometer is secured in place, and the three centering micrometer screws in the stage IV vacuum chamber are adjusted until the laser beam is seen to emerge clearly

through the window at the upper end of the spectrometer. At this point the ionizer inlet aperture and stage III exit aperture are lined up correctly. The collimator assembly is then positioned and adjusted to pass the laser beam. Similarly the skimmer assembly is added and brought into alignment. Finally, the sampling orifice assembly is put in place and positioned to pass the laser beam.

When the sampling apparatus is pumped down and put into operation, the sampling orifice position is given a final "fine tuning" adjustment. This adjustment is made while ambient laboratory air is being sampled. The mass filter is set on the maximum of the nitrogen peak and the electrometer output on the recorder is observed while adjusting the sampling orifice centering screws in flange L. Adjustments are made to maximize the nitrogen signal.

#### Spectrometer Tuning

The quadrupole mass spectrometer used in our apparatus is one for which all settings of the ionizing, focusing, and mass filtering elements must be determined by the experimenter. The detection of low level signals depends very strongly upon the adjustment of these elements. Optimum adjustment corresponds to maximizing the signal-to-noise ratio (S/N) rather than just maximizing the signal.

Our experience has indicated that the two controls which most strongly affect maximization of S/N are the emission current and the ion energy. Although in general the signal strength increases as each of these parameters is increased, a point is reached where the noise level begins to increase more rapidly than the signal level. We have found that optimum S/N is achieved at relatively low emission current (typically about 3 mA) and ion energy (typically 10 V at 32 AMU).

Tuning is accomplished by observing an intense peak on the oscilloscope and adjusting the controls to produce the proper peak shape. This is usually done by observing the nitrogen peak while sampling ambient laboratory air. A fast repetitive sweep rate is used and the resolution control is set to a low value so that the peak covers several AMU and is about 8 centimeters wide on the oscilloscope screen. The tuning controls are adjusted so that the top of the peak is flat, the high mass side of the peak is vertical, and the low mass side is a straight line with maximum slope. These features of the peak shape are sought while also endeavoring to maintain as large a peak amplitude as possible. The ideal shape is shown in figure 20 by the heavy solid line. Once the tuning is optimized, the resolution can be increased considerably before the peak amplitude is affected. As the resolution is increased, the position of the low mass side of the peak should move toward higher mass as shown by the dashed lines in figure 20. When the low mass side of the peak just intercepts the high mass side, e.g., point A in figure 20, the spectrometer is tuned to the highest resolution which gives the maximum S/N. Increasing the reso-

lution control further increases the resolution but only at the expense of a loss in sensitivity, e.g., point B in figure 20.

Optimum resolution and sensitivity at low AMU does not necessarily represent the optimum at high AMU. The control which most strongly affects the ratio of the low to high AMU resolution is the  $\Delta M$  control. We have found that for our spectrometer a setting of  $\Delta M = 0$  should be used to obtain resolutions which are equally satisfactory at low and high AMU while maintaining good sensitivity.

The intensity and resolution are usually checked daily by observing a one atmosphere oxygen beam. The oxygen used contains a low level xenon impurity which provides a suitable signal at relatively high AMU. The oxygen peak and one of the xenon peaks are alternately observed while fine tuning.

Typical resolutions (defined using the full-width at half-maximum), used when detecting low level signals, are 1X to 2X the mass number in the AMU region near xenon and 2X the mass number in the region near oxygen.

#### Beam Modulation

Fite (ref. 44) has pointed out that in selecting a chopping frequency for performing modulated beam mass spectrometric measurements two physical considerations govern. First, the frequency should be made sufficiently high to insure that the Fourier component of the background gas pressure fluctuations is negligibly small. Second, the frequency should be made sufficiently low to insure that coherence of the modulated beam is not destroyed as the result of velocity spreading of the beam pulses.

For effusive molecular beams where there is a broad distribution of velocities, the second consideration above is of critical importance. Fite and Brackman (ref. 45), Harrison et al. (refs. 46 and 47), and Yomamoto and Stickney (ref. 48) have analyzed the effusive beam case and worked out the dependence of the amplitude and phase shift on frequency, molecular mass and flight path length.

For supersonic beams, Miller (ref. 49) has shown that the second consideration above is not critical. Miller showed that amplitude corrections are minor when the Mach number is greater than about 5. This results from the fact that at high Mach numbers the velocity distribution is sufficiently narrow that the spread in velocities does not effect the coherence of the beam even at relatively high chopping frequencies, e.g., 1400 hertz.

Because our sampling system produces a high Mach number supersonic beam, we have only considered background gas pressure fluctuation effects in selecting a chopping frequency. We have used the analysis of Fite (ref. 44) to estimate the ratio of amplitudes of pressure fluctuations,

in the stage II vacuum chamber, for a chopped beam as compared to an unchopped beam. The stage II vacuum system's time constant is approximately 40 milliseconds. At a chopping frequency of 150 hertz the pressure fluctuation amplitude is attenuated by a factor of about 40 and at a frequency of 400 hertz the attenuation factor is 100.

### RESULTS AND DISCUSSION

The general performance of our sampling system was initially assessed by sampling the ambient laboratory atmosphere through a 0.025 centimeter diameter orifice. The orifice-to-skimmer distance was arbitrarily set at  $X_s/D_0 = 50$ . These initial tests demonstrated that the vacuum pumping systems met the design criteria and were adequate for ambient temperature, atmospheric pressure sampling through a 0.025 centimeter diameter orifice. The pressure in stage I was about 1.5 microns, and this value corresponds to the region where the 10-inch diffusion pumps begin to achieve their maximum pumping speed. This result indicates that the 0.025 centimeter diameter orifice is about the maximum that can be used on our sampler with the stage I pumping provided. The pressure in stages II, III, and IV was  $2 \times 10^{-5}$ ,  $3 \times 10^{-7}$ , and  $< 10^{-8}$  torr, respectively.

A portion of a typically recorded spectrum for the laboratory ambient atmosphere is shown in figure 21. The peaks at 32, 33, 34 AMU are due to oxygen and those at 36, 38, and 40 AMU are due to argon which exists in the atmosphere at about 0.93 percent by volume. An estimate of the sampling system's sensitivity was ascertained by observing that the  $Ar^{38}$  isotope was readily identified and measured here with the spectrometer and electronics set to only an intermediate sensitivity level. This isotope is of the order of 5 parts per million (ppm) in the ambient atmosphere.

The 37 AMU peak in figure 21 was attributed to the ion species  $H(H_2O)_2^+$ . A subsequent scan of ambient air was made to higher AMU and is shown in figure 22. This scan was at a higher sweep rate and lower sensitivity than that shown in figure 21. The water and water cluster peaks are clearly visible and in accord with observations made by other investigators (ref. 50). To confirm these observations we sampled ambient air which was first passed through a drying column. A scan of the dry air sample is shown in figure 23. The water peak at 18 AMU is seen to be greatly reduced and the water cluster peaks are absent. The scans shown in figures 22 and 23 were made at the same sensitivity, scan speed and time constant. At higher sensitivity, slower scan speed and increased time constant the dried air sample still showed some water clustering peaks and this demonstrated that, as expected, the drying was not complete.

After the preliminary testing described above, experiments were performed to determine (1) how measured intensity varied as a function of  $X_s/D_0$  and source pressure,  $P_0$ , (2) how the measured intensity of an argon beam compared to theoretically calculated intensity, and (3) the ultimate sensitivity of the sampling system. For these experiments the translat-

able sampling orifice assembly was installed on the sampler. Experiments were performed with argon, nitrogen, and oxygen as the room temperature source gas.

### Argon

Argon was sampled at various source pressures and the in-phase ion current was measured as a function  $X_s/D_0$ . Typical results at three source pressures are presented in figure 24. The intensity of the argon signal is seen to pass through a rather broad maximum near  $X_s/D_0 = 120$  and then fall sharply at lower values of  $X_s/D_0$ . The sharp drop in intensity at lower orifice to skimmer distances is similar to that reported by other investigators (ref. 51), and this drop is usually attributed to skimmer interference and shock effects (refs. 51 and 52). We believe that in our case the drop in intensity at low values of  $X_s/D_0$  may also be due to background gas scattering effects because at small orifice-to-skimmer distances the pumping in the region of the orifice is probably somewhat restricted. The gradual decrease in intensity at  $X_s/D_0$  values beyond the maximum may be due to the decreased density at the skimmer entrance resulting from the increasing orifice-to-skimmer separation. According to the idealized theoretical analysis of Parker et al. (ref. 36), the flux at the detector varies as  $(X_s/D_0)^{-2/3}$  for argon. This is in reasonable agreement with our observations for  $X_s/D_0$  values greater than where the maximum intensity occurs.

It is interesting to note that if one makes a simplistic calculation of a skimmer Knudsen number at the point of maximum intensity, a value is obtained which is about equal to that usually considered to be a criteria for free molecular flow. For example, consider the case of argon with  $P_0 = 700$  torr and  $X_s/D_0 = 120$ . As will be shown later, the number density at the skimmer is calculated to be  $n_s = 2.35 \cdot 10^{14}$  atoms-cm<sup>-3</sup>. The mean free path at the skimmer,  $\lambda_s$ , is calculated to be 0.71 centimeter from the expression  $\lambda_s = (\sqrt{2} \pi \sigma^2 n_s)^{-1}$  where the collision cross section  $\sigma$  is taken to have the value  $3.67 \cdot 10^{-8}$  cm. For the 0.076 centimeter skimmer diameter, the skimmer Knudsen number,  $Kn_s$ , is calculated from  $Kn_s = \lambda_s/D_s$  to be 9.3. Because a value of  $Kn_s = 10$  is taken as the criteria for free molecular flow, it is reasonable to conclude that for our example free molecular flow prevailed where maximum intensity was achieved. Upstream of where free molecular flow prevails, collisions still play a role and shock or scattering effects would be expected to attenuate the beam as previously postulated. Thus this qualitative picture in general can explain the experimentally observed shapes of the intensity versus  $X_s/D_0$  curves. Furthermore, this approach is in general accord with the findings of other investigators who observed similar curve shapes (refs. 53 and 54). For example, Scott and Drewry (ref. 54) concluded that experimental results rise to a maximum and tend to approach theoretical predictions as  $Kn_s$  increases.

Our measured dependence of intensity on source pressure for  $X_S/D_0 = 120$  is shown in figure 25. For pressures below about 600 torr the intensity is seen to be directly proportional to source pressure and this is in accord with theoretical considerations. The fall-off of intensity at higher pressures was not expected. We speculated that this might be related to stage I pumping. At these higher pressures the stage I pressure is in the region where the diffusion pumps just begin to attain their maximum pumping speed. However, the stage I pressure is almost linearly related to source pressure, as shown in figure 26, even to source pressures of 800 torr. One would expect to see a departure from linearity at higher pressures if the diffusion pumps were not pumping at their maximum speed.

Pressures in stages II, III, and IV were measured as a function of source pressure and  $\lambda_S/D_0$ . For all conditions the stage IV pressure was always less than  $10^{-8}$  torr and this fact demonstrates that even for argon the stage IV pumping capacity was more than adequate. The pressures measured in stages II and III were found to be a function of source pressure and  $X_S/D_0$  as shown in figure 27 where results are presented for two source pressures.

To compare measured intensities with theoretically calculated values it is necessary to relate measured ion current to beam flux or number density which can be expressed in terms of source conditions. Because the ion source of the mass spectrometer is a density sensitive detector, we chose to characterize the beam in terms of number density  $n$ . The centerline number density at the ion source,  $n_d$ , is proportional to the measured ion current,  $I$ ,

$$n_d = CI \quad (43)$$

where  $C$  is the proportionality constant and the current is the in-phase component of the modulated beam current. The proportionality constant may be a function of molecular species but for any given species, such as argon, the proportionality should be equally applicable to an effusive or supersonic beam. If the effusive beam is subscripted by  $E$  and the supersonic (nozzle) beam is subscripted by  $N$ , we can write for a particular species  $i$ ,

$$i^C = \frac{i^n d_E}{i^I E} = \frac{i^n d_N}{i^I N} \quad (44)$$

Effusive argon beams were produced by sampling argon source gas at pressures in the micron range and the results are shown in figure 28. Generally, effusive flow is considered to exist for orifice Knudsen numbers above about 10 but our data was found to be very linear to source pressures near 400 microns where the Knudsen number is approximately 0.5. The data to  $P_0 = 400$  microns was fitted to a straight line by the least squares method and the line shown through the data points in figure 28 was found to fit the equation,

$$Ar I_E = 1.95 \times 10^{-12} Ar P_0 - 1.04 \times 10^{-2} \quad (45)$$

At a source pressure of 30 microns the number density at the detector (ion source) was calculated to be  $Ar n_{dE} = 1.81 \cdot 10^7$  molecules  $cm^{-3}$

for  $X_s/D_0 = 120$  and a skimmer-to-detector distance,  $l$ , equal to 42.82 centimeters. From the least squares line equation a source pressure of 30 microns results in a beam current of  $5.75 \times 10^{-11}$  ampere. The proportionality constant  $ArC$  is then calculated to be  $ArC = 3.15 \cdot 10^{17}$  molecules  $cm^{-3}$  ampere $^{-1}$ .

Supersonic argon beams resulting from a source pressure of 700 torr were measured as a function of  $X_s/D_0$  and the measured ion currents,  $Ar I_N$ , were converted to number density,  $Ar n_{dN}$ , by multiplying  $Ar I_N$  by  $ArC$ . Results are presented in figure 29 where it can be seen that the maximum density occurs at  $X_s/D_0 = 120$  where  $Ar n_{dN} = 3.07 \cdot 10^{11}$  molecules  $cm^{-3}$ .

Theoretical densities at the detector can be calculated by equation (35) and the techniques described in the section on Beam Formation. Calculations were made for the source conditions  $P_0 = 700$  torr of argon,  $T_0 = 298$  K,  $D_0 = 0.025$  centimeter,  $X_s/D_0 = 120$ ,  $D_s = 0.038$  centimeter, and  $l = 42.82$  centimeters. When  $M_{I_S}$  was calculated according to equation (37) [ $M_{I_S} = M_T(X_s/X_q)$ ] and the first method, we obtained

$Ar n_{dN} = 1.03 \cdot 10^{12}$  molecules  $cm^{-3}$  for a theoretical density. This value is a factor of about 3.4 higher than our measured value. When  $M_{I_S}$  was calculated according to the second method and equation (42)

( $M_{I_S} = (2.50/\sqrt{\gamma})(X_s/D_0)\{D_0/(\tau_0 c_0)^{-0.2}\}$ ), we obtain  $Ar n_{dN} = 3.24 \cdot 10^{11}$

molecules  $cm^{-3}$  which is only about 5 percent higher than our measured value. It must be recognized that while both theories are based on many idealized assumptions, the second method calculation results from a theory derived from correlations with experiment. Therefore, it is not surprising that the density derived from the second calculation is in better agreement with our measurements.

For either method of calculation of the theoretical density at the detector, the agreement with experiment is considered to be good and an indication that at  $X_s/D_0 = 120$  skimmer interference is not a serious problem in our apparatus. The calculations also yield additional information which gives some insights into the sampler's operation. For the source conditions noted  $M_T = 30.2$  and the transition to "collisionless flow" occurs near  $X_q/D_0 = 28$  where  $n_q = 4.26 \cdot 10^{15}$  molecules  $cm^{-3}$ . The density at skimmer is  $n_s = 2.35 \cdot 10^{14}$  molecules  $cm^{-3}$ .

A final series of argon beam experiments were performed to ascertain if abnormal condensation effects existed in our sampling system beam formation process. Condensation phenomenon are an important consideration

in high pressure sampling and extensive research (refs. 55 to 58 and references cited therein) has been devoted to this subject. While most aspects of condensation in free jets is beyond the scope of our discussion, Milne and Greene (ref. 55) have shown how measurement of the argon dimer to monomer ratio can be used to evaluate the performance of a sampler.

Argon source gas was sampled at room temperature through a 0.025 centimeter diameter orifice. Orifice-to-skimmer distance was held constant at the optimum determined previously, i.e.,  $X_s/D_0 = 120$ . In-phase ion currents were measured for the argon monomer and dimer. Measured ion currents were not corrected for mass spectrometer mass discrimination, multiplier gain or sampler mass discrimination because such corrections were considered to be relatively small for the short range from 40 to 80 AMU.

At a source pressure of one atmosphere we measured an argon dimer to monomer ratio of  $3.6 \times 10^{-3}$ . This value is in good agreement with Milne and Greene's data (ref. 55, fig. 5) extrapolated to our orifice size. We therefore conclude that for the orifice size, source pressure and temperature, and orifice-to-skimmer distance used we had a relatively undisturbed free-jet expansion and beam formation.

### Nitrogen

Nitrogen was used as a source gas to perform experiments similar to those done with argon. The results obtained with nitrogen were generally the same as those obtained with argon. Pressures in the various vacuum chambers as a function of source pressure and  $X_s/D_0$  were in substantial agreement with those measured with argon as the source gas. Intensity also varied with  $P_0$  and  $X_s/D_0$  in a fashion similar to argon. Effusion experiments yielded a value for the proportionality constant  $N_2C = 2.97 \times 10^{17}$  molecules  $\text{cm}^{-3}$  ampere $^{-1}$ . The measured density at the detector,  $N_2 n_{dN}$ , is plotted as a function of  $X_s/D_0$  in figure 30 for a source pressure of 700 torr. Again the density is seen to pass through a broad maximum which peaks at  $X_s/D_0 = 120$ . The maximum density for nitrogen is  $1.26 \times 10^{11}$  molecules  $\text{cm}^{-3}$ .

The maximum density measured at the detector for argon beams is about a factor of 2.5 higher than that measured for nitrogen beams under the same conditions. If one calculates a theoretical density by the methods of equation (35), a higher density is obtained for nitrogen compared with argon. The value of such calculations for nitrogen are, however, somewhat suspect because the theoretical equations were developed mainly on the basis of a monatomic gas.

### Oxygen

Preliminary experiments with oxygen as the source gas indicated that a xenon impurity contained in the oxygen might be useful for determining the ultimate sensitivity of our sampling system. Therefore, a number of

experiments were performed with oxygen. Missile grade tank oxygen was used at atmospheric pressure with a 0.025 centimeter sampling orifice diameter and with  $X_s/D_0 = 120$ . The oxygen was independently analyzed by conventional mass spectrometric techniques which had a sensitivity of about 1 ppm. No xenon was detected in that analysis and we therefore took the xenon level to be 1 ppm.

When the oxygen was sampled with our sampling system xenon was readily identified. A typically recorded spectrum of the xenon isotopes is given in figure 31. The total current (upper trace) was obtained at maximum spectrometer sensitivity for acceptable resolution, i.e., maximum electron multiplier gain and maximum electrometer sensitivity. The major xenon isotopes are just discernible and for the 132 isotope the signal-to-noise ratio is about 2. However, the in-phase current (lower trace) clearly shows the xenon isotopes and the signal-to-noise ratio for the 132 isotope is about 10. The in-phase current was measured with the lock-in amplifier sensitivity set a factor of 10 below maximum and a 10 second time constant was used. Figure 31 demonstrates the signal-to-noise ratio enhancement that is achieved by beam modulation and phase sensitive detection. Had a longer time constant and slower scan rate been used, an even greater enhancement could have been attained.

The 132 xenon isotope is about one fourth of the total xenon level and thus for the presumed xenon impurity level of 1 ppm the 132 signal represents about 0.25 ppm. Clearly, if the 132 signal were one fourth the level shown in figure 31, it would still be easily measurable at the sensitivities employed. On this basis we therefore expect an ultimate sensitivity for our sampling system in this general mass range to be on the order of 0.05 ppm.

#### Other Source Gas Systems

We have used our sampling apparatus to study reaction product formation in flames and flowing gas systems (ref. 13) as well as to study volatile products emanating from metal samples subjected to various gaseous environments at elevated temperatures (refs. 14 and 15). For these experiments atmospheric pressure gases were sampled through a 0.022 centimeter diameter orifice in the apex of a 0.6 centimeter high sampling cone welded to a 2 centimeter diameter by 1.5 centimeter high stainless steel tube attached to the flange plate. The skimmer diameter was 0.081 centimeter and  $X_s/D_0 = 144$ . For this arrangement the stage I and II pressures were  $1.5 \times 10^{-3}$  and  $8 \times 10^{-6}$  torr, respectively, with room temperature atmospheric pressure source gas. When the gas temperature was 1000° C, these pressures were  $7 \times 10^{-4}$  and  $1 \times 10^{-6}$  torr, respectively. Stage III and IV pressures were less than  $10^{-7}$  and  $10^{-8}$  torr, respectively, for both source gas temperatures.

Flat flames were produced with a specially designed burner (ref. 13) and fuel-lean methane-oxygen flames doped with  $SO_2$ ,  $H_2O$ , and  $NaCl$  were

used to study the formation of  $\text{Na}_2\text{SO}_4(\text{g})$ . Gaseous flame reaction products were measured by recording the in-phase ion current at appropriate values of AMU. Composition profiles were determined by measuring each species ion current as a function of vertical distance between the sampling orifice and burner surface, denoted by  $Z$ . Clogging of the sampler orifice by condensible species was a problem which limited the duration of each sampling experiment to about 30 minutes.

Measured composition profiles for a 9.5 mole ratio  $\text{O}_2/\text{CH}_4$  flame doped with  $\text{SO}_2$ ,  $\text{H}_2\text{O}$ , and  $\text{NaCl}$  are presented in figure 32. The profiles observed for  $\text{O}_2$ ,  $\text{H}_2\text{O}$ , and  $\text{CO}_2$  are similar to those reported by other investigators for  $\text{CH}_4\text{-O}_2$  flames (ref. 59). The direct observation of  $\text{Na}_2\text{SO}_4(\text{g})$ ,  $\text{NaSO}_2(\text{g})$ , and  $\text{NaSO}_3(\text{g})$  are new findings and the shape of their profiles is discussed in reference 13.

The formation of  $\text{Na}_2\text{SO}_4(\text{g})$  was also studied in a flowing gas reaction tube system at 1413 K. The reaction tube was positioned at the sampler inlet in such a way that the sampling orifice on the stainless steel tube extended into the reaction tube and the hot zone. The orifice was allowed to get hot before the water-saturated oxygen,  $\text{SO}_2$  and  $\text{NaCl}(\text{g})$  were flowed through the hot reaction zone.

Intensities were measured for the gaseous species  $\text{O}_2$ ,  $\text{H}_2\text{O}$ ,  $\text{SO}_2$ ,  $\text{SO}_3$ ,  $\text{NaCl}$ ,  $\text{Na}_2\text{SO}_4$ , and  $\text{NaSO}_3$  with known flows of  $\text{O}_2$ ,  $\text{SO}_2$ ,  $\text{H}_2\text{O}$ , and known concentrations of  $\text{NaCl}(\text{g})$ . The species  $\text{NaOH}(\text{g})$  and  $\text{HCl}(\text{g})$  with parent ions at  $m/e$  40 and 36, 38 could not be measured because large in-phase background peaks were present at these  $m/e$  values. These background peaks were due to argon which is a 2300 ppm impurity in the missile grade oxygen that was used.

Equilibrium thermodynamic calculations of the composition of the reaction products were made as a function of temperature. In the calculations the composition of the reactants was held constant at the weight fractions 0.96  $\text{O}_2$ ,  $1.2 \times 10^{-5}$   $\text{NaCl}$ , 0.012  $\text{H}_2\text{O}$ , and 0.032  $\text{SO}_2$ . Calculated reaction product ion intensity fractions are compared with the equilibrium calculated mole fractions in the histogram shown in figure 33.

Considering that the measured intensities were not corrected for sampling factors, the quality of agreement between experiment and calculation is considered quite good.

Our sampler has proven to be valuable in studying the atmospheric pressure oxidation of various metals subjected to various contaminant gases added to the oxygen environment (refs. 14 and 15). The high pressure mass spectrometric sampling technique has been used to identify volatile products emanating from the metal samples. For these experiments the metal specimen is suspended in the reaction tube and the sampling orifice is located 1 to 2 centimeters above the specimen. An example of the type of results obtained is shown in figure 34 for the system chromium specimen plus  $\text{O}_2 + \text{NaCl}(\text{g}) \pm \text{H}_2\text{O}(\text{g})$  at  $1020^\circ \text{C}$ . With this system the new species  $(\text{NaCl})_x\text{CrO}_3$  with  $x = 1, 2, \text{ or } 3$ ,  $(\text{NaOH})_y\text{CrO}_3$  with  $y = 1 \text{ or } 2$ ,

$\text{NaClNa}_2\text{Cr}_2\text{O}_7$ , and  $\text{NaOENa}_2\text{Cr}_2\text{O}_7$  were readily identified. At first glance one might suspect that these complexes are the product of gas phase reactions occurring in the sampling process, but independent evidence (ref. 14) suggests that this is not the case. Even in the case of the NaCl polymers condensation clustering does not seem reasonable when one considers the low NaCl(g) pressure and the fact that the gas is at elevated temperature (ref. 60).

#### ACKNOWLEDGMENTS

The authors are indebted to Dr. John Dillard who performed the argon and nitrogen beam experiments.

#### REFERENCES

1. Stringer, J.: Hot Corrosion in Gas Turbines. MCIC 72-08, Metals and Ceramics Information Center, 1972.
2. Hart, Anthony B.; and Cutler, A. J. B., ed.: Deposition and Corrosion in Gas Turbines. John Wiley & Sons, Inc., 1973.
3. Fairbanks, J. W.; and Machlin, I., eds.: Proceedings of the 1974 Gas Turbine Materials in the Marine Environment Conference. MCIC 75-27, Metals and Ceramics Information Center, 1975. (Available from DDC as AD-AD13436.)
4. Milne, Thomas A.; Vandergrift, A. Eugene, and Greene, Frank T.: Mass-Spectrometric Observations of Argon Clusters in Nozzle Beams. II. The Kinetics of Dimer Growth. J. Chem. Phys., vol. 52, no. 3, Feb. 1970, pp. 1552-1560.
5. Milne, Thomas A.; Beachey, Jacob E.; and Greene, Frank T.: Study of Relaxation in Free Jets Using Temperature Dependence of n-Butane Mass Spectra. J. Chem. Phys., vol. 56, no. 6, Mar. 1972, pp. 3007-3013.
6. Milne, Thomas A.; Beachey, Jacob E.; and Greene, Frank T.: Vaporization Kinetics and Thermodynamics of Graphite Using the High Pressure Mass Spectrometer. Rep. 3518C, Midwest Res. Inst., (AFML-TR-72-227, AD-753713), Dec. 1972.
7. Biordi, Joan C.; Lazzara, Charles P.; and Papp, John F.: Molecular Beam Mass Spectrometry Applied to Determining the Kinetics of Reactions in Flames. II. A Critique of Rate Coefficient Determinations. Combust. Flame, vol. 26, no. 1, Feb. 1976, pp. 57-76.
8. Farber, Milton; and Srivastava, R. D.: Thermochemical Reactions of Aluminum and Fluorine in Hydrogen-Oxygen Flames. Combust. Flame, vol. 27, no. 1, Aug. 1976, pp. 99-105.

9. Hayhurst, A. N.; and Telford, N. R.: Mass Spectrometric Sampling of Ions from Atmospheric Pressure Flames. I: Characteristics and Calibration of the Sampling System. *Combust. Flame*, vol. 28, no. 1, 1977, pp. 67-80.
10. Hastie, J. W.: Sampling Reactive Species from Flames by Mass Spectrometry. *Int. J. Mass Spectrom. Ion Phys.*, vol. 16, 1975, pp. 89-100.
11. Young, W. S., et al.: Molecular-Beam Sampling of Gases in Engine Cylinders. *Technology Utilization Ideas for the 70's and Beyond*, AAS Sci. Technol. Ser., vol. 26, F. W. Forbes and P. Dergarabedian, eds., American Astronaut. Soc., 1971, pp. 281-289.
12. Goshgarian, B.; Selph, C.; and O'Pray, J.: Mass Spectrometric Investigation of Fluorocarbon Flames. AIAA paper 74-1141, Oct, 1974.
13. Stearns, Carl A., et al.: Gaseous Sodium Sulfate Formation in Flames and Flowing Gas Environments. NASA TM X-73600, 1977.
14. Stearns, Carl A.; Kohl, Fred J.; and Fryburg, George C.: Reactions of Chromium with Gaseous NaCl in an Oxygen Environment. NASA TM X-73476, 1976.
15. Fryburg, George C., et al.: Volatile Products in the Corrosion of Cr, Mo, Ti and Four Superalloys Exposed to O<sub>2</sub> Containing H<sub>2</sub>O and Gaseous NaCl. NASA TM X-73599, 1977.
16. Diesen, R. W.: Mass-Spectral Studies of Kinetics Behind Shock Waves. III. Thermal Dissociation of Fluorine, *J. Chem. Phys.*, vol. 44, no. 10, May 15, 1966, pp. 3662-3666.
17. Williams, G. J.; and Wilkins, R. G.: An Investigation of the Chemical Structure of Perchloric Acid Flames. Part I - The Molecular Beam Sampling Apparatus, *Combust. Flame*, vol. 21, no. 3, Dec. 1973, pp. 325-337.
18. Dushman, Saul: *Scientific Foundations of Vacuum Technique*. John Wiley & Sons, Inc., 1949.
19. Anderson, J. B.: *Molecular Beams from Nozzle Sources. Molecular Beams and Low Density Gas Dynamics*, Peter P. Wegener, ed., Marcel Dekker, Inc., 1974, pp. 1-91.
20. Bier, K.; and Hagena, O. F.: Influence of Shock Waves on the Generation of High-Intensity Molecular Beams by Nozzles. *Rarefied Gas Dynamics, Proc. of Third Int. Symp.*, vol. 1, J. A. Laurmann, ed., Academic Press, 1963, pp. 478-496.
21. Ashkenas, Harry; and Sherman, Frederick S.: The Structure and Utilization of Supersonic Free Jets in Low Density Wind Tunnels. *Rarefied Gas Dynamics, Proc. of Fourth Int. Symp.*, vol. 2, J. H. de Leeuw, ed., Academic Press, 1966, pp. 84-105.
22. Knuth, Eldon L.: Supersonic Molecular Beams. *Appl. Mech. Rev.*, vol. 17, no. 10, Oct. 1964, pp. 751-762.

23. Anderson, J. B.; Andres, R. P.; and Fenn, J. B.: Supersonic Nozzle Beams. *Advances in Chemical Physics*, vol. X, Molecular Beams, John Ross, ed., Interscience Publishers, 1966, pp. 275-317.
24. Anderson, J. B.; Andres, R. P.; and Fenn, J. B.: High Intensity and High Energy Molecular Beams. *Advances in Atomic and Molecular Physics*, vol. 3, David R. Bates and I. Estermann, eds., Academic Press, 1965, pp. 345-385.
25. Knuth, Eldon L.: Direct-Sampling Studies of Combustion Processes. Engine Emissions: Pollutant Formation and Measurement, George S. Springer and Donald J. Patterson, eds., Plenum Publishing Co., 1973, pp. 319-363.
26. Hansen, Arthur G.: *Fluid Mechanics*. John Wiley & Sons, Inc., 1967.
27. Knuth, Eldon L.: Rotational and Translational Relaxation Effects in Low-Density Hypersonic Free Jets. Dept. Eng. Rep. 64-53, Univ. of California, Los Angeles, 1964.
28. Anderson, J. B., et al.: Studies in Low-Density Supersonic Jets. Rarefied Gas Dynamics, Proc. of Fourth Int. Symp., vol. 2, J. H. de Leeuw, ed., Academic Press, 1966, pp. 106-127.
29. Milne, Thomas A.; and Greene, Frank T.: Mass-Spectrometric Sampling of 1-Atm. Flames. Tenth Symposium (International) on Combustion, The Combustion Institute, 1965, pp. 153-159.
30. Calo, J. M.: Dimer Formation in Supersonic Water Vapor Molecular Beams. *J. Chem. Phys.*, vol. 62, no. 12, June 15, 1975, pp. 4904-4910.
31. Anderson, James B.: Separation of Gas Mixtures in Free Jets. *AIChE J.*, vol. 13, no. 6, Nov. 1967, pp. 1188-1192.
32. Milne, Thomas A.; and Greene, Frank T.: Molecular Beams in High Temperature Chemistry. *Advances in High Temperature Chemistry*, vol. 2, Leroy Eyring, ed., Academic Press, 1969, pp. 107-150.
33. Bird, G. A.: Breakdown of Translational and Rotational Equilibrium in Gaseous Expansions. *AIAA J.*, vol. 8, no. 11, Nov. 1970, pp. 1998-2003.
34. Anderson, J. B.; and Fenn, J. B.: Velocity Distributions in Molecular Beams from Nozzle Sources. *Phys. Fluids*, vol. 8, no. 5, May 1965, pp. 780-787.
35. Kantrowitz, Arthur; and Grey, Jerry: A High Intensity Source for the Molecular Beam. Part I. *Theoretical Rev. Sci. Instrum.*, vol. 22, no. 5, May 1951, pp. 328-332.
36. Parker, H. M.; Kuhlthau, A. R.; and Zapata, R.: The Application of Supersonic Beam Sources to Low-Density, High-Velocity Experimentation. *Rarefied Gas Dynamics, Proc. First Int. Symp.*, F. M. Devienne, ed., Pergamon Press, 1960, pp. 69-79.
37. LeRoy, Rodney L.; and Govers, Thomas F.: "Ideal" Intensities of Supersonic Molecular Beams. *Can. J. Chem.*, vol. 48, no. 11, June 1, 1970, pp. 1743-1747.

38. Hagen, Otto F.; and Morton, Harold S., Jr.: Analysis of Intensity and Speed Distribution of a Molecular Beam From a Nozzle Source. *Rarefied Gas Dynamics, Proc. of Fifth Int. Symp.*, vol. II, C. L. Brundin, ed., Academic Press, 1967, pp. 1369-1384.
39. French, J. B.: Molecular Beams for Rarefied Gas Dynamic Research. AGARDOGRAPH-112, 1966.
40. LeRoy, Rodney L.; Govers, Thomas R.; and Deckers, Jacques M.: Supersonic Molecular Beam Intensities. *Can. J. Chem.*, vol. 48, no. 6, Mar. 15, 1970, pp. 927-933.
41. Hamel, Bernard B.; and Willis, D. Roger: Kinetic Theory of Source Flow Expansion with Application to the Free Jet. *Phys. Fluids*, vol. 9, no. 5, May 1966, pp. 829-841.
42. Sharma, P. K.; Knuth, E. L.; and Young, W. S.: Species Enrichment Due to Mach-number Focusing in a Molecular-Beam Mass-Spectrometer Sampling System. *J. Chem. Phys.*, vol. 64, no. 11, June 1, 1976, pp. 4345-4351.
43. Habets, A. H. M.; Beijerinck, H. C. W.; and Verster, N. F.: Perpendicular-Temperature Measurements on a Cryopumped Supersonic Argon Jet. *Rarefied Gas Dynamics, Proc. of Ninth Int. Symp.*, vol. 1, M. Becker and M. Fiebig, eds., DFVLR Press, 1974, pp. B-6-1 to 6-11.
44. Fite, W. L.: Selection of Frequency in Modulated Beam Mass Spectrometry. Extranuclear Laboratories, Inc., Res. Note 2.
45. Fite, Wade L.; and Brackman, R. T.: Collisions of Electrons with Hydrogen Atoms. I. Ionization. *Phys. Rev.* 112, no. 4, Nov. 15, 1958, pp. 1141-1151.
46. Harrison, Halstead; Hummer, David G.; and Fite, Wade L.: Velocity Dispersion of Square-Modulated Maxwellian Molecular Beams. *J. Chem. Phys.*, vol. 41, no. 7, 1964, pp. 2567-2568.
47. Harrison, H.; Hummer, D. G.; and Fite, W. L.: Velocity Dispersion of Square-Modulated Maxwellian Molecular Beams: The Integral
- $$F_N(x) = \int_0^{\infty} y^n \exp(-y^2 - ix/y) dy.$$
- Scientific Memo 26, Boeing Sci. Res. Labs., 1963.
48. Yamamoto, S.; and Stickney, R. E.: Analysis of "Lock-In" Detection of Modulated Molecular Beams Scattered From Solid Surfaces. *J. Chem. Phys.*, vol. 47, no. 3, Aug. 1, 1967, pp. 1091-1099.
49. Miller, R. A.: Crossed Molecular Beam Reactive Scattering of Barium and Samarium with Sulfur Dioxide. Ph. D. Thesis, Case Western Reserve Univ., 1976.
50. Milne, Thomas A.; Beachey, Jacob E.; and Greene, Frank T.: A Direct Mass Spectrometric Study of the Formation and Reactions of Water-Cluster Ions. AFCRL-70-034½, Midwest Res. Inst., 1970. (Available from DDC as AD-709229.)

51. Bossel, Ulf: Investigation of Skimmer Interaction Influences on the Production of Aerodynamically Intensified Molecular Beams. Ph. D. Thesis, Univ. of California, Berkeley, 1968 (see also Office of Naval Research Report AS-68-6).
52. McLean, W. J.: Direct Mass Spectrometric Sampling From High Pressure Systems. Ph. D. Thesis, Univ. of California, Berkeley, 1971.
53. Fenn, John B.; and Deckers, Jacques: Molecular Beams From Nozzle Sources., Rarefied Gas Dynamics, Proc. Third Int. Symp., vol. 1, J. A. Laurmann, ed., Academic Press, 1963, pp. 497-515.
54. Scott, John E., Jr.; and Drawry, James E.: Characteristics of Aerodynamic Molecular Beams. Rarefied Gas Dynamics, Proc. Third Int. Symp., vol. 1, J. A. Laurmann, ed., Academic Press, 1963, pp. 516-538.
55. Milne, Thomas A.; and Greene, Frank T.: Mass Spectrometric Observations of Argon Clusters in Nozzle Beams. I. General Behavior and Equilibrium Dimer Concentrations. J. Chem. Phys., vol. 47, no. 10, Nov. 15, 1967, pp. 4095-4101.
56. Milne, Thomas A.; Greene, Frank T.; and Beachey, Jacob E.: Detection of Argon Cluster Fragmentation in a Time-of-Flight Mass Spectrometer. J. Chem. Phys., vol. 56, no. 11, June 1, 1972, pp. 5340-5342.
57. Beylich, A. E.: Theoretical Investigation of the Argon Dimerization. Rarefied Gas Dynamics, Proc. of Ninth Int. Symp., M. Becker and M. Fiebig, eds., DEVL Press, 1974, pp. F5-1-F5-10.
58. Hagena, O. F.: Cluster Beams From Nozzle Sources. Molecular Beams and Low Density Gasdynamics, Peter P. Wegener, ed., Marcel Depper, Inc., 1974, pp. 93-181.
59. Peeters, Jozef; and Mahnen, Gilbert: Reaction Mechanisms and Rate Constants of Elementary Steps in Methane-Oxygen Flames. Fourteenth Symp. Int. on Combustion, The Combustion Institute, 1973, pp. 133-146.
60. Hagena, O. F.; and Obert, W.: Cluster Formation in Expanding Supersonic Jets: Effect of Pressure, Temperature, Nozzle Size and Test Gas. J. Chem. Phys., vol. 56, no. 5, Mar. 1, 1972, pp. 1793-1802.

TABLE I. - MACH NUMBER EXPANSION

## EQUATION CONSTANTS

$\gamma$	$X_0/D_0$	A
5/3	0.075	3.26
7/5	.04	3.65
9/7	.85	3.96

TABLE II. - POLYNOMIALS FOR EXTRAPOLATING MACH NUMBER

## TO SUBSONIC FLOW REGIME

$\gamma$	Range	Polynomial
5/3	$0 \leq (X/D_0) \leq 1.665$	$M = 1.000 + 1.671(X/D_0) + 0.047_1(X/D_0)^3$
5/3	$-0.897_7 \leq (X/D_0) \leq 0$	$M = 1.000 + 1.671(X/D_0) - 0.691_2(X/D_0)^3$
7/5	$0 \leq (X/D_0) \leq 2.228$	$M = 1.000 + 1.441(X/D_0) - 0.019_0(X/D_0)^3$
7/5	$-1.041 \leq (X/D_0) \leq 0$	$M = 1.000 + 1.441(X/D_0) - 0.443_3(X/D_0)^3$
9/7	$0 \leq (X/D_0) \leq 2.852$	$M = 1.000 + 1.174(X/D_0) - 0.015_0(X/D_0)^3$
9/7	$-1.278 \leq (X/D_0) \leq 0$	$M = 1.000 + 1.174(X/D_0) - 0.239_8(X/D_0)^3$

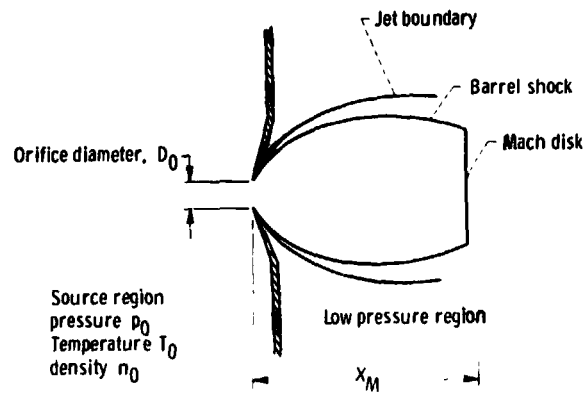


Figure 1. - Free-jet expansion shock structure.

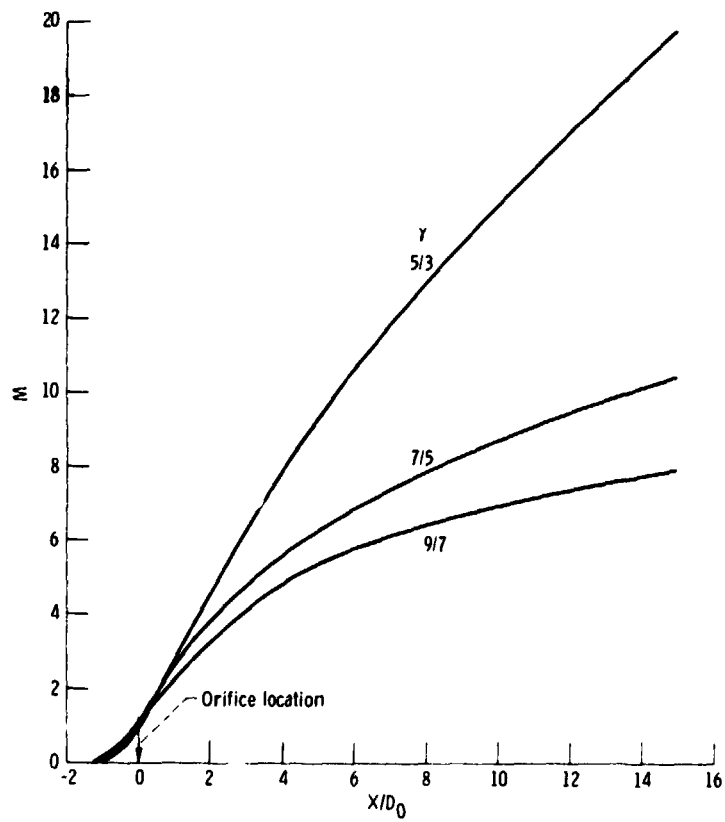


Figure 2. - Mach number variation with downstream distance,  $X/D_0$ , for three values of the specific heat ratio  $\gamma$ .

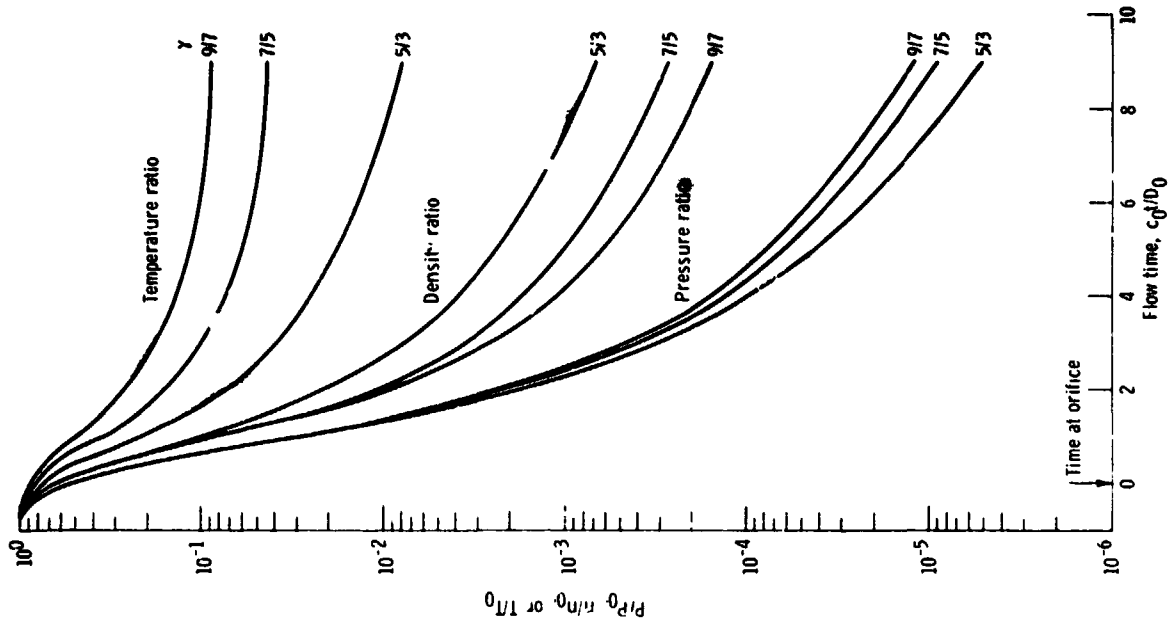


Figure 4. - Variation of pressure, density, and temperature with dimensionless flow time for three values of the specific heat ratio  $\gamma$ .

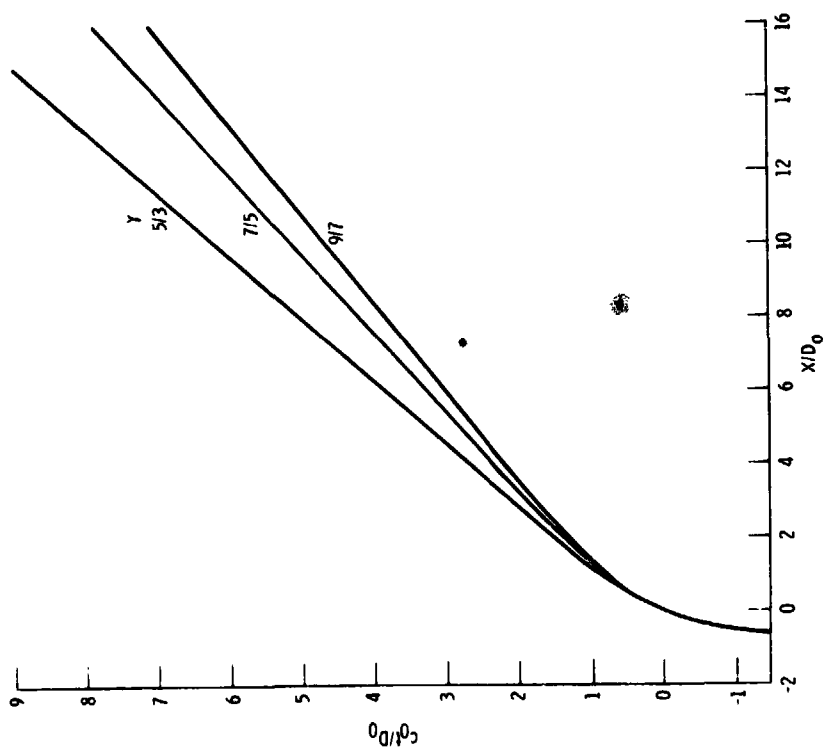


Figure 3. - Dimensionless flow time  $c_0^2/D_0$  variation with downstream distance,  $X/D_0$  for three values of the specific heat ratio  $\gamma$

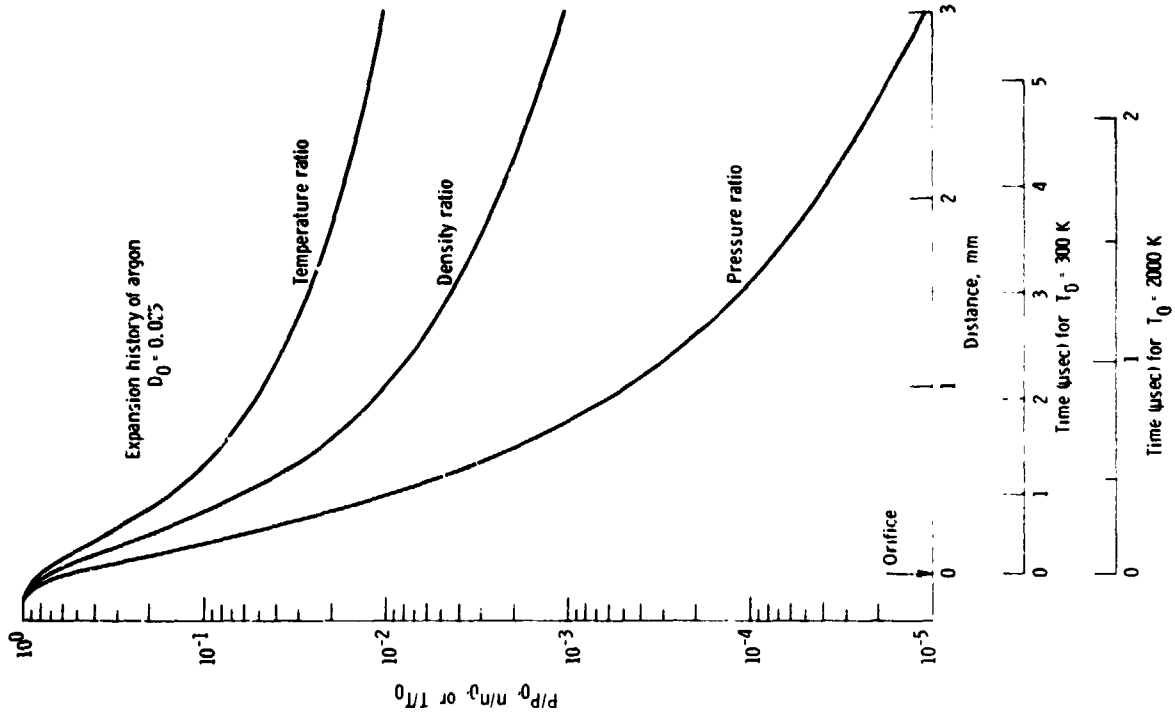


Figure 6 - Expansion history of argon source gas.

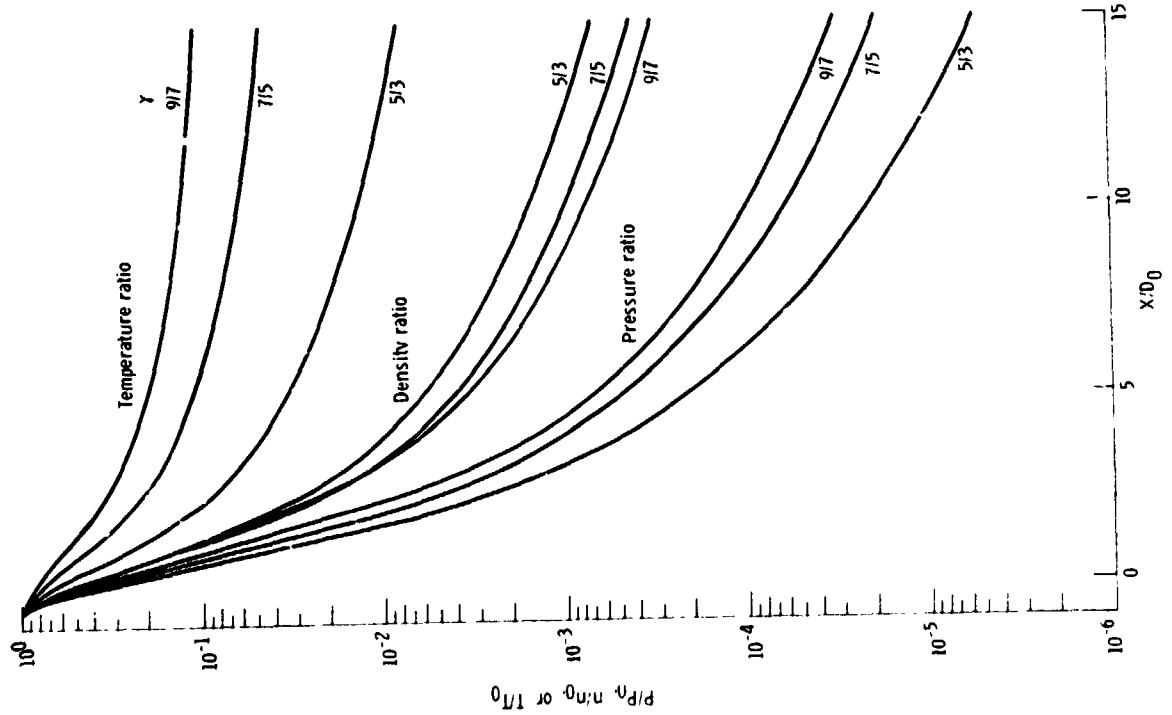


Figure 5 - Variation of pressure, density, and temperature with downstream distance for three values of the specific heat ratio  $\gamma$

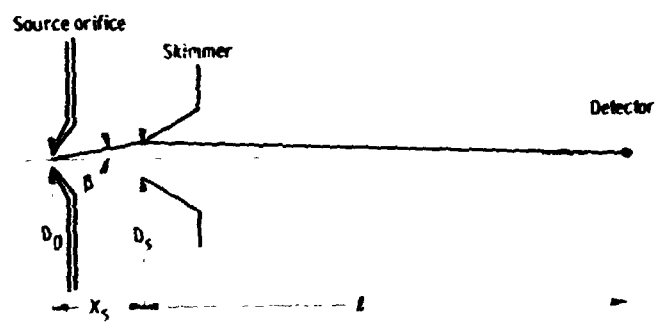


Figure 7. - Orifice, skimmer, detector geometry.

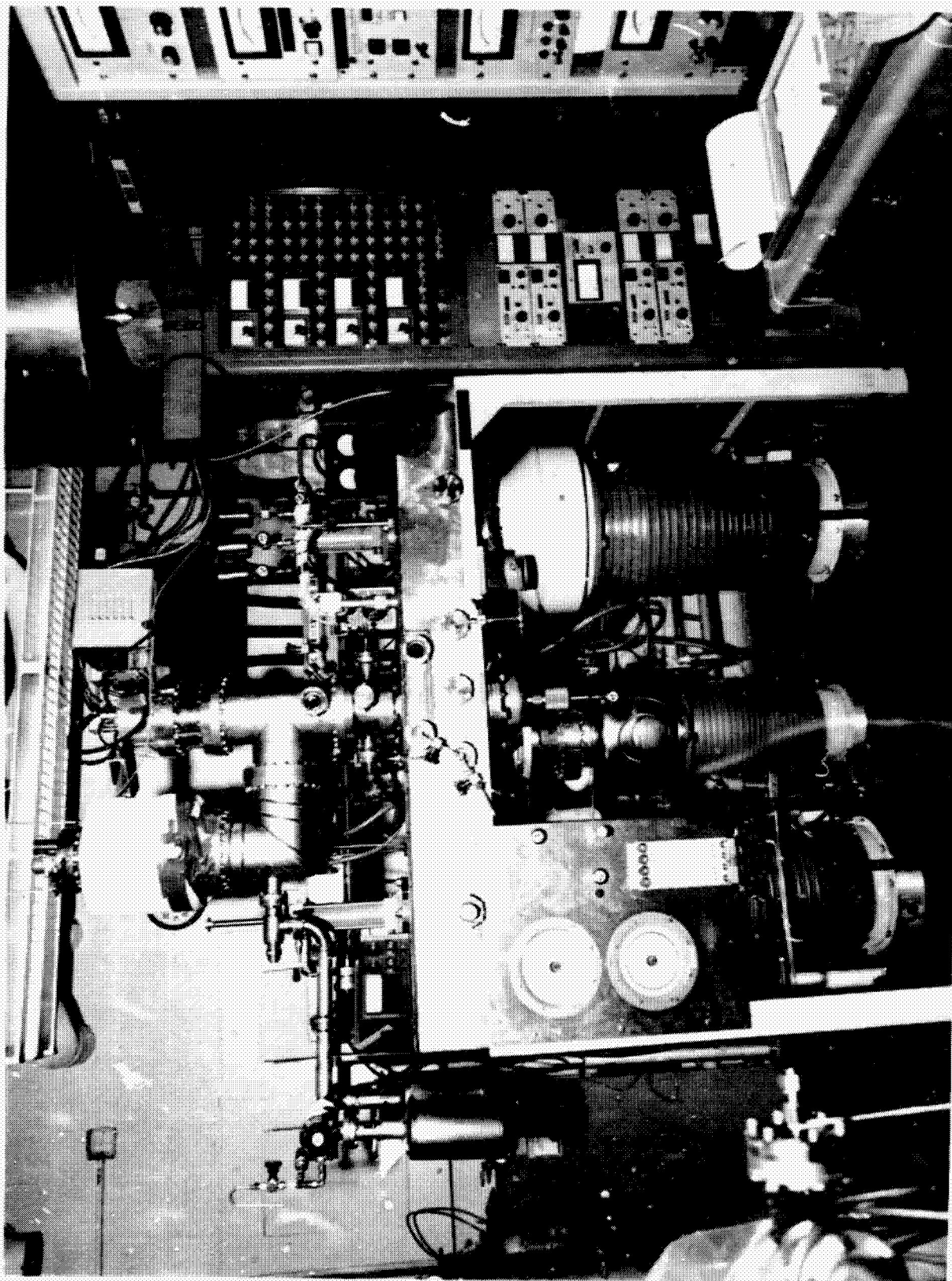


Figure 8. - Photograph of high pressure mass spectrometric sampling apparatus.

REPRODUCTION OF THE  
ORIGINAL PAGE IS POOR

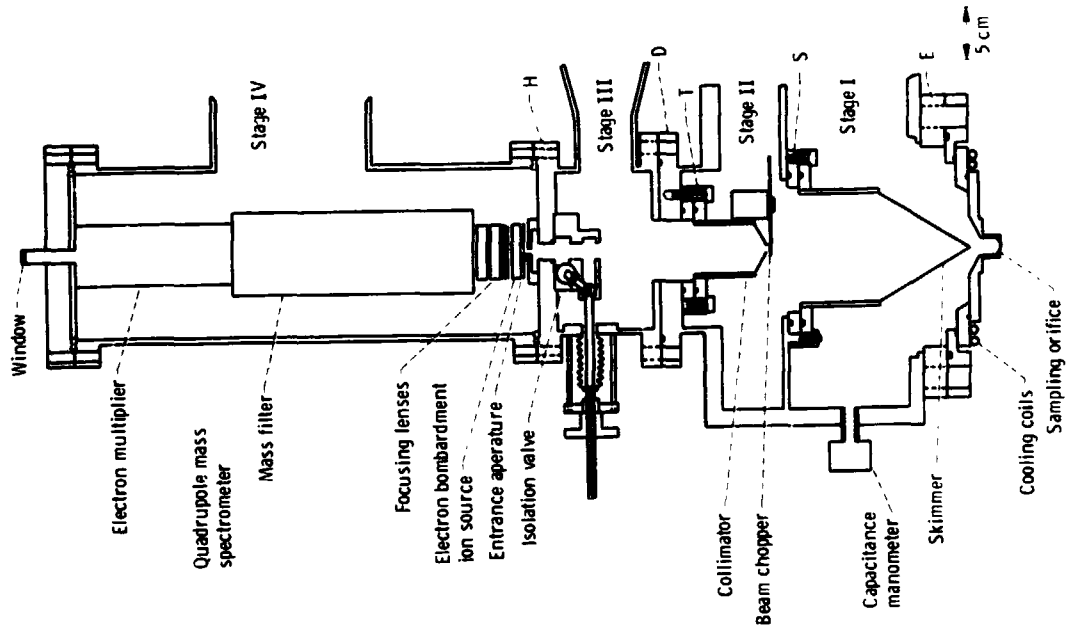


Figure 9. - Schematic cross section of high pressure mass spectrometric sampler.

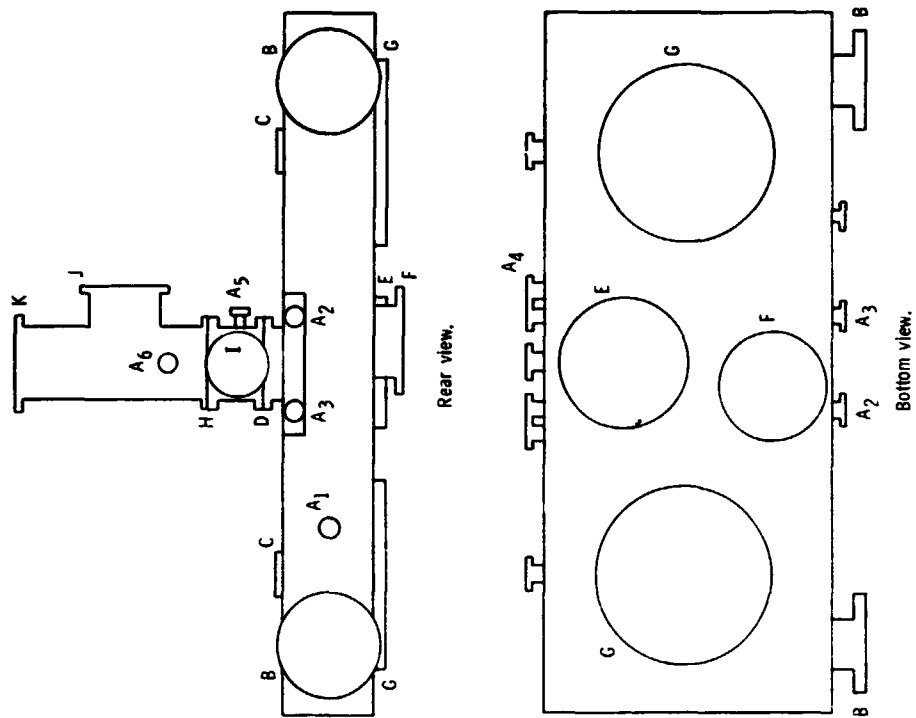


Figure 10. - Schematic views of sampler vacuum chambers.

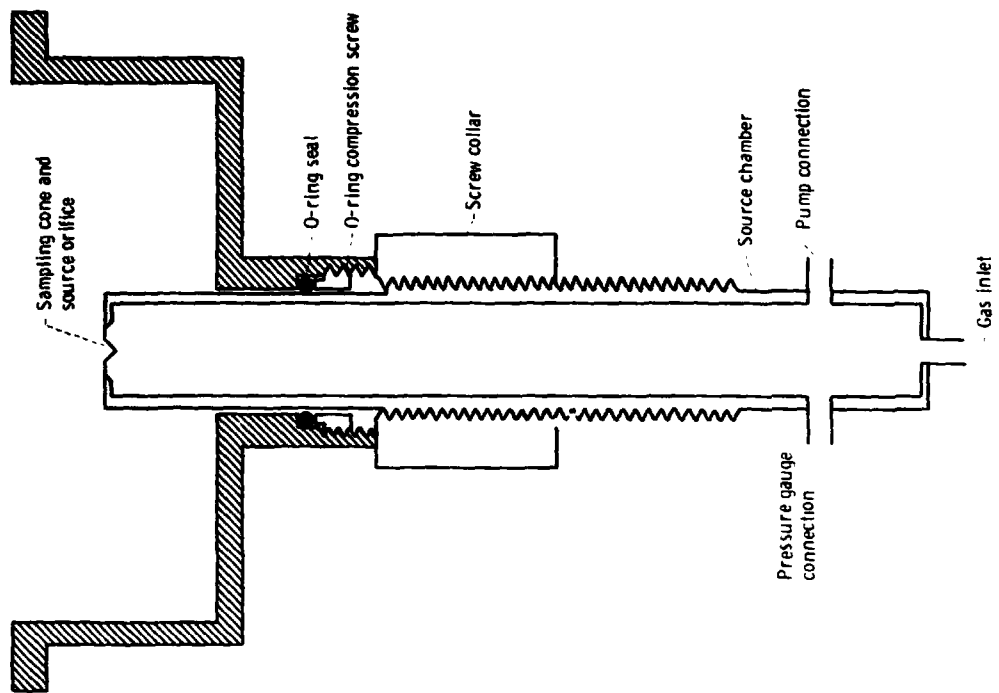
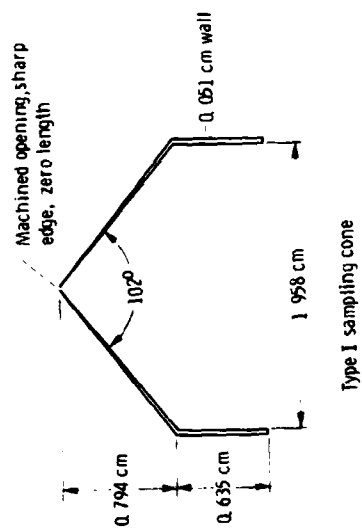
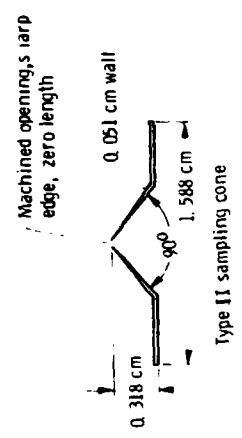


Figure 13. - Schematic cross-sectional view of translatable orifice inlet assembly.



Type I sampling cone



Type II sampling cone

Figure 12. - Types of sampling orifice cones.

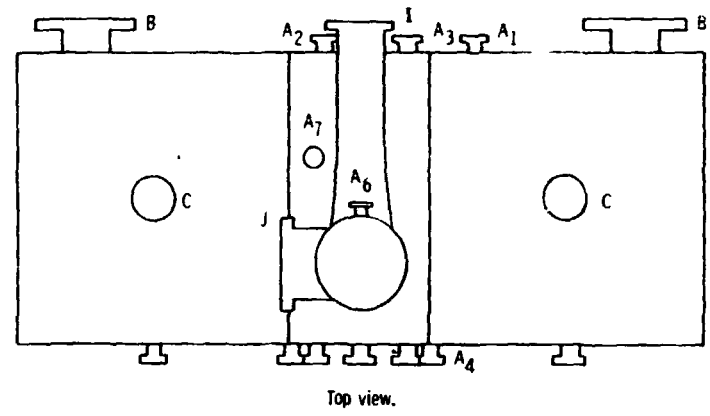
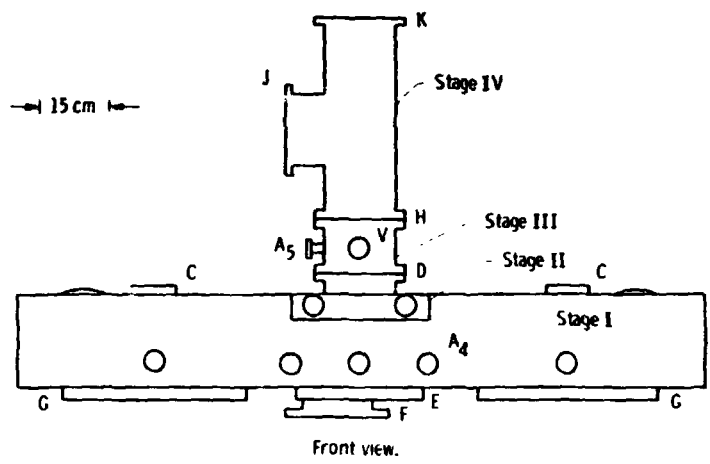


Figure 10. - Concluded.

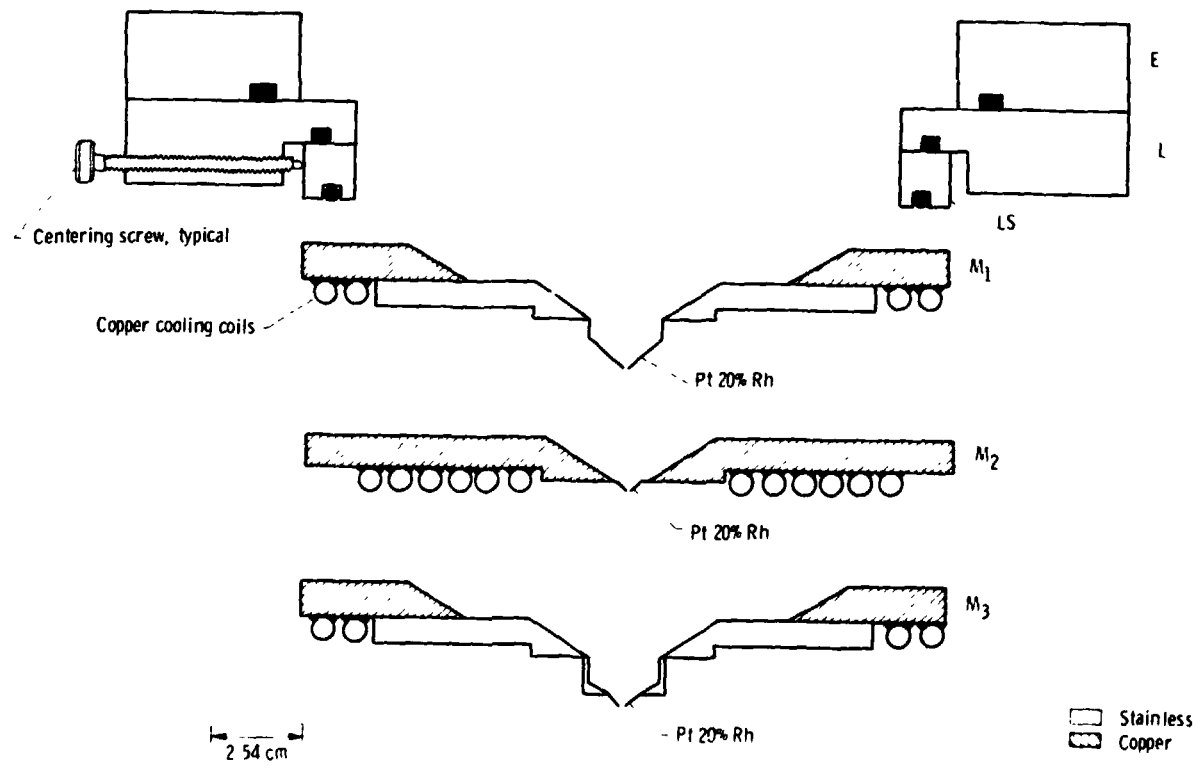


Figure 11. - Schematic cross-sectional views of various sampling orifice inlet assemblies.

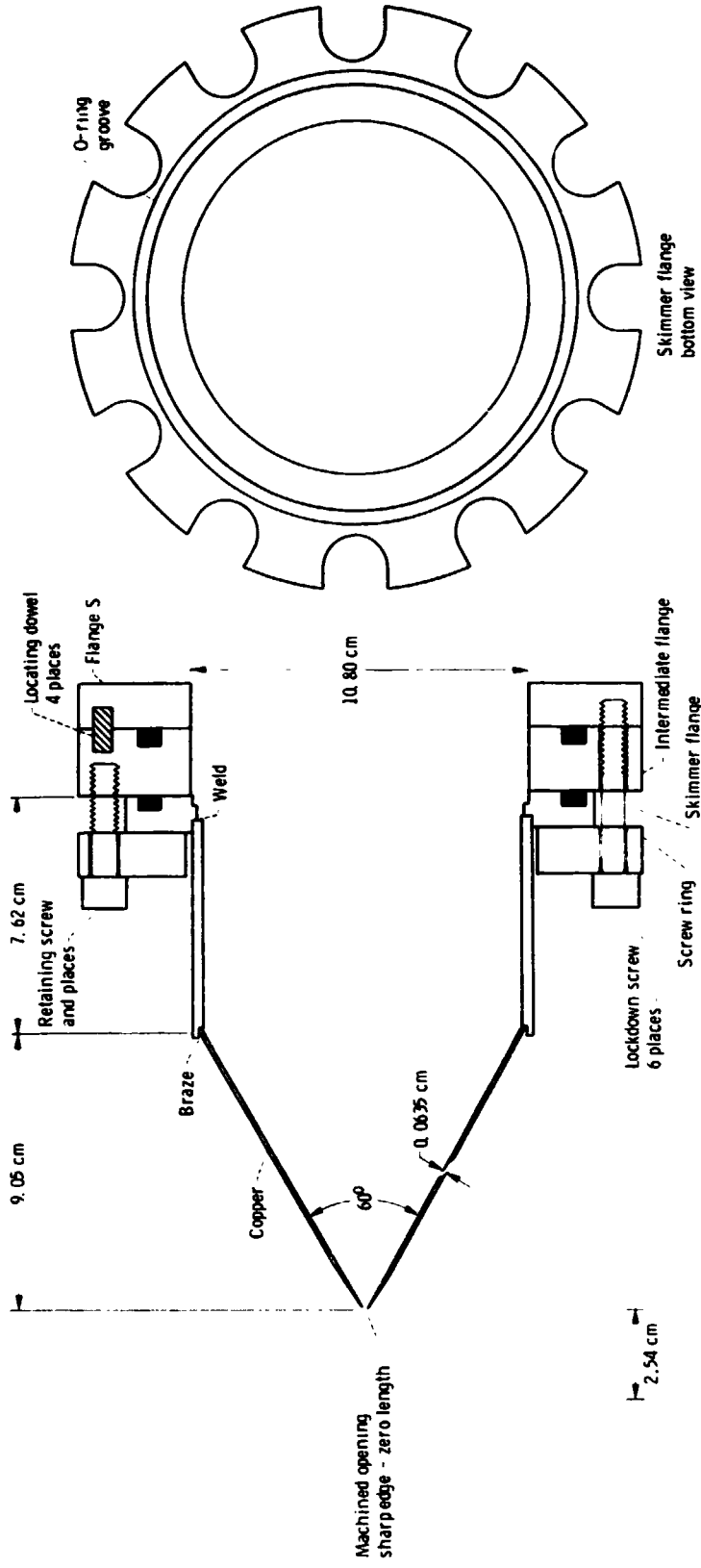


Figure 14. Skimmer assembly.

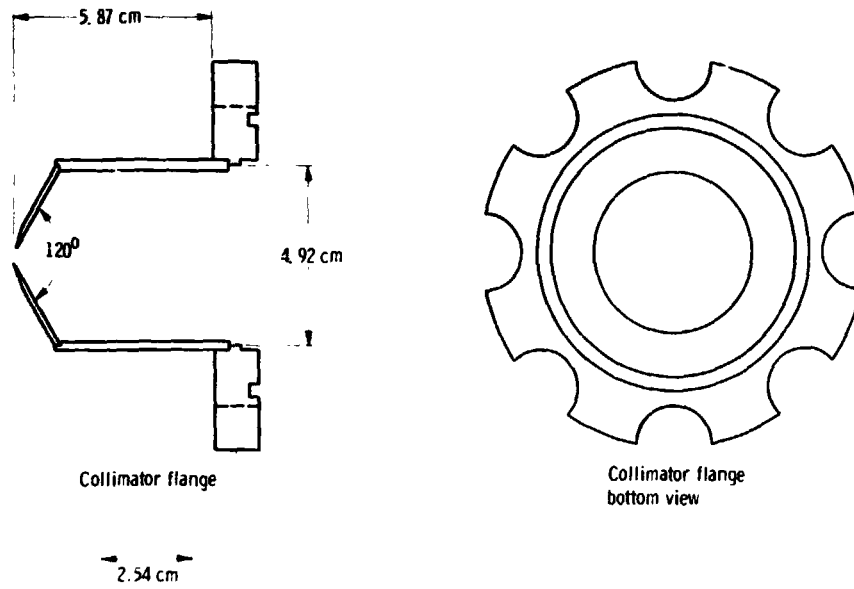


Figure 15. - Collimator.

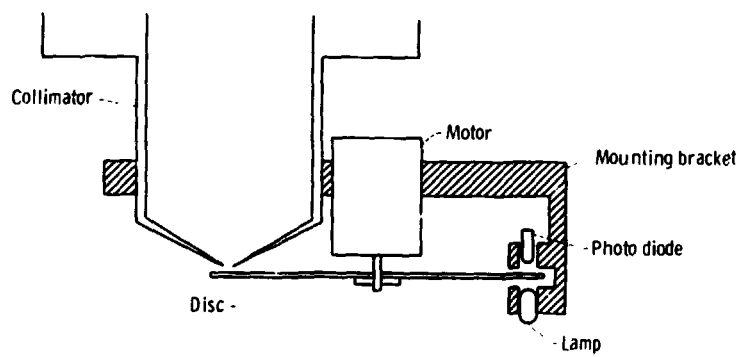


Figure 16. - Beam chopper assembly.

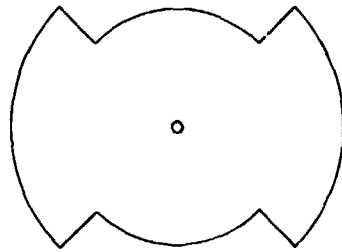


Figure 17. - Beam chopper segmented disc.

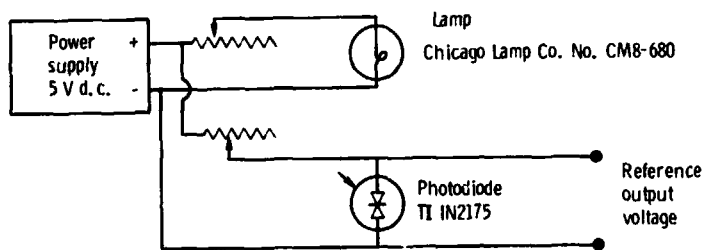
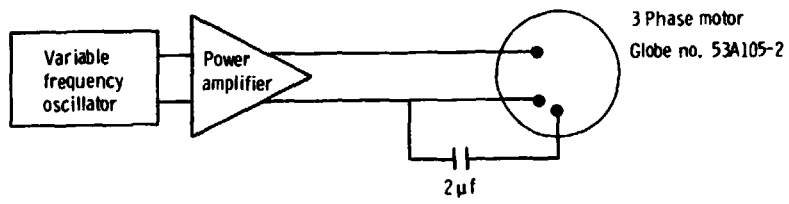


Figure 18. - Schematic wiring di. gram for chopper system.

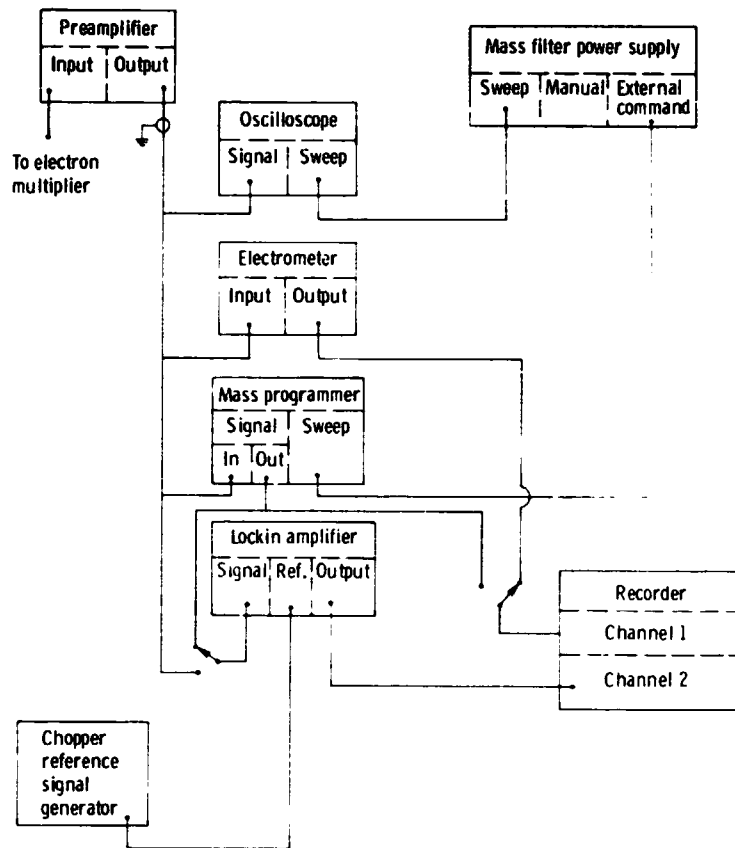


Figure 19. - Block diagram of signal and control channels.



Figure 20. - Idealized focusing peak shape.

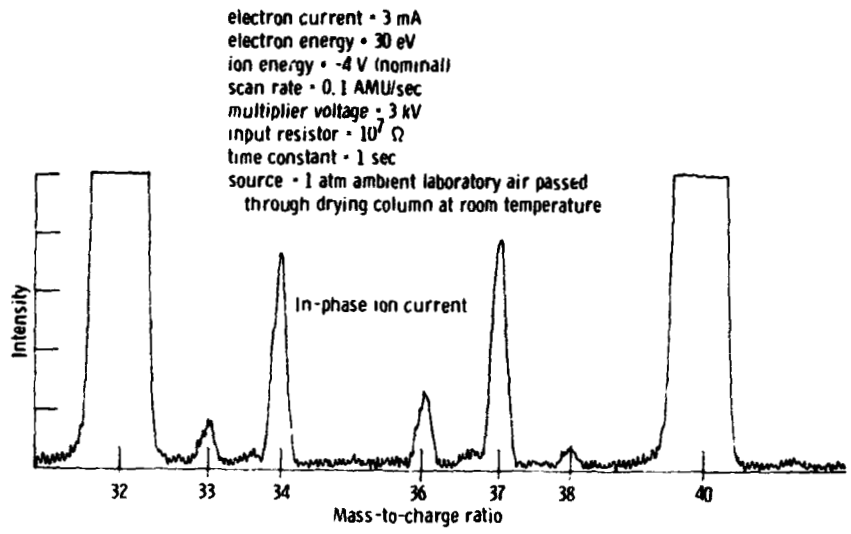


Figure 21. - Portion of mass spectral scan for ambient laboratory air.

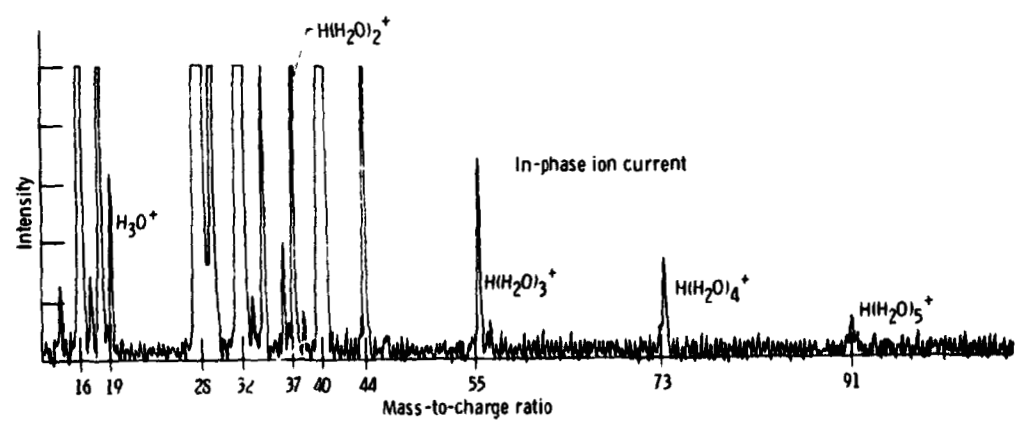


Figure 22. - Mass spectral scan of ambient laboratory air.

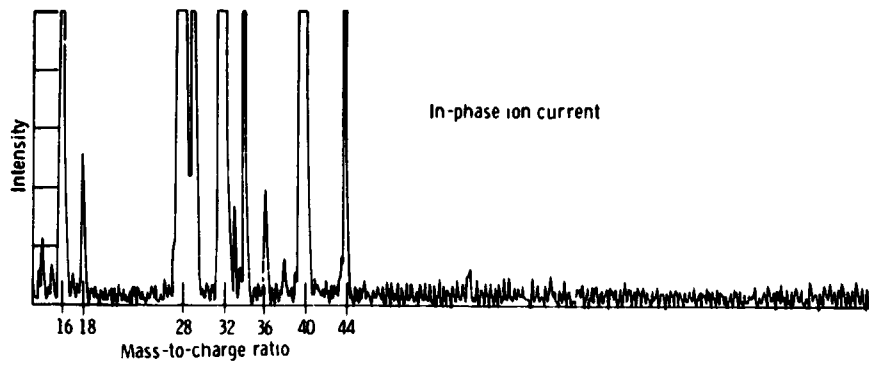


Figure 23. - Mass spectral scan of ambient laboratory air passed through drying column.

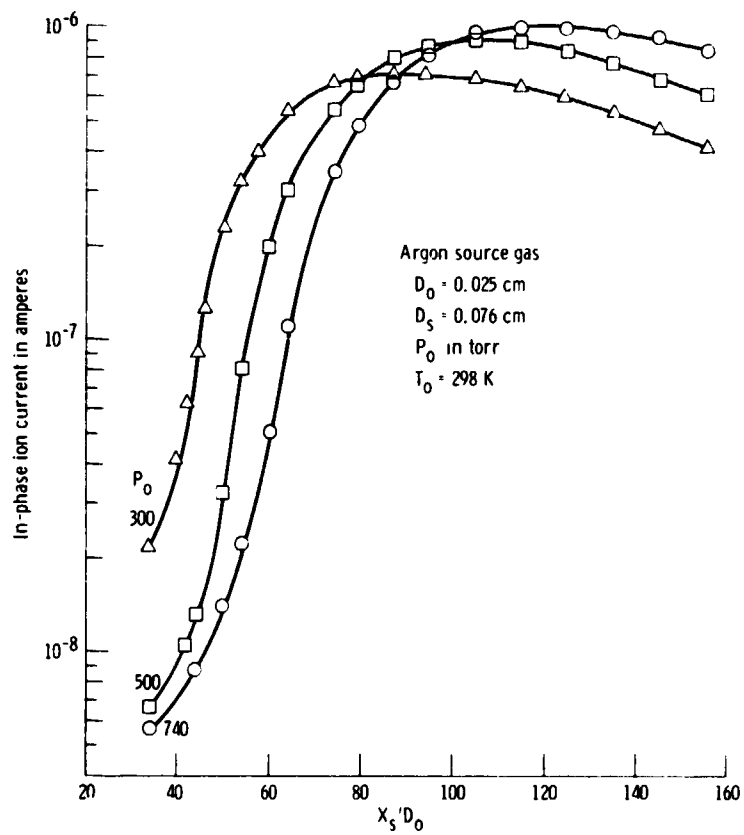


Figure 24. - Argon beam intensity variation as a function of orifice-to-skimmer distance and source pressure.

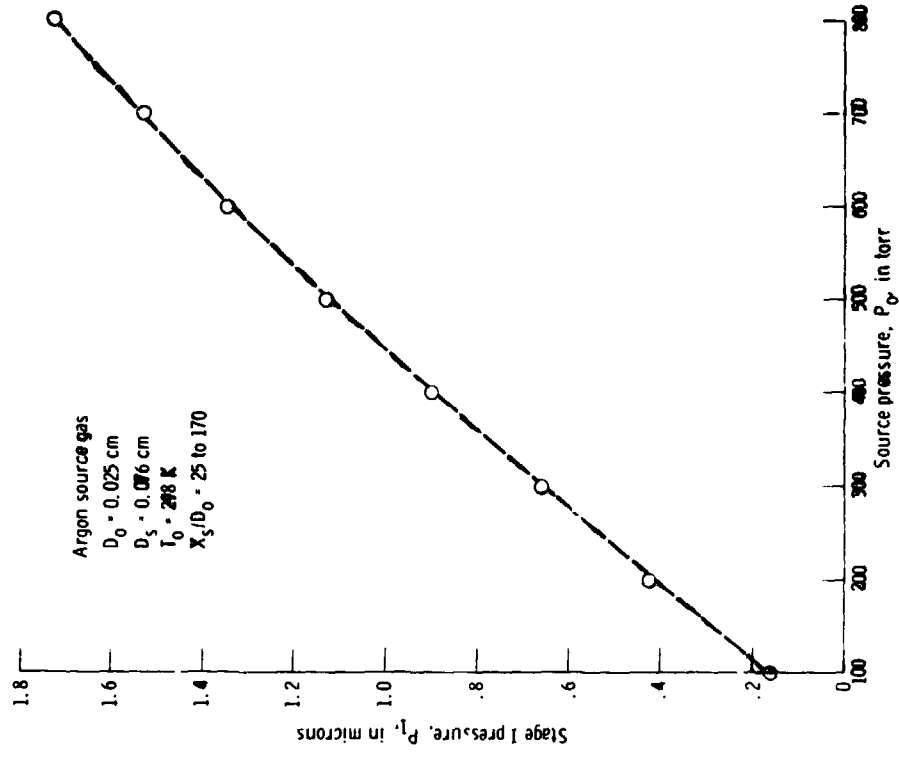


Figure 26. - Variation of first stage expansion pressure as a function of source pressure.

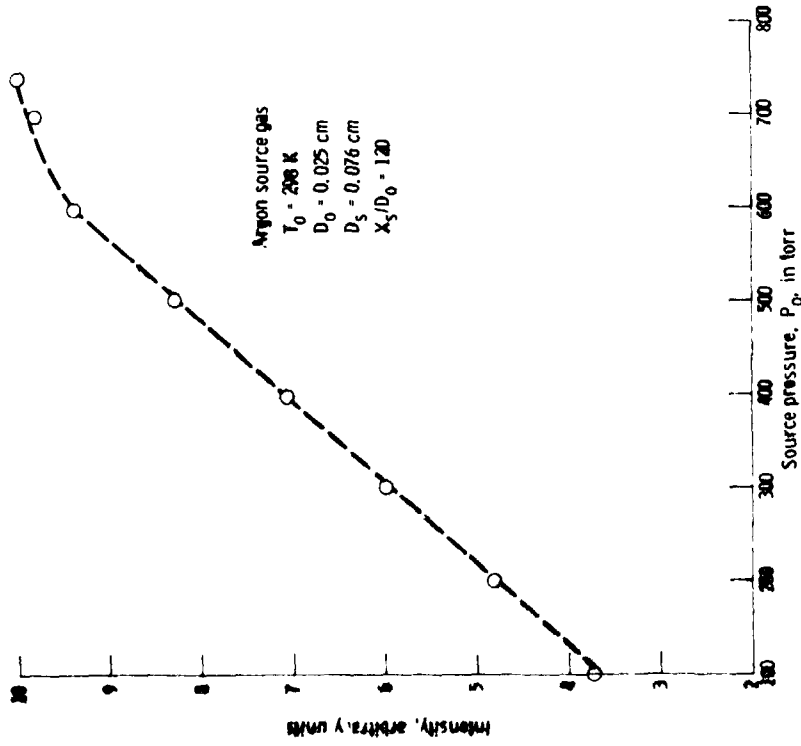


Figure 25. - Argon beam intensity variation with source pressure.

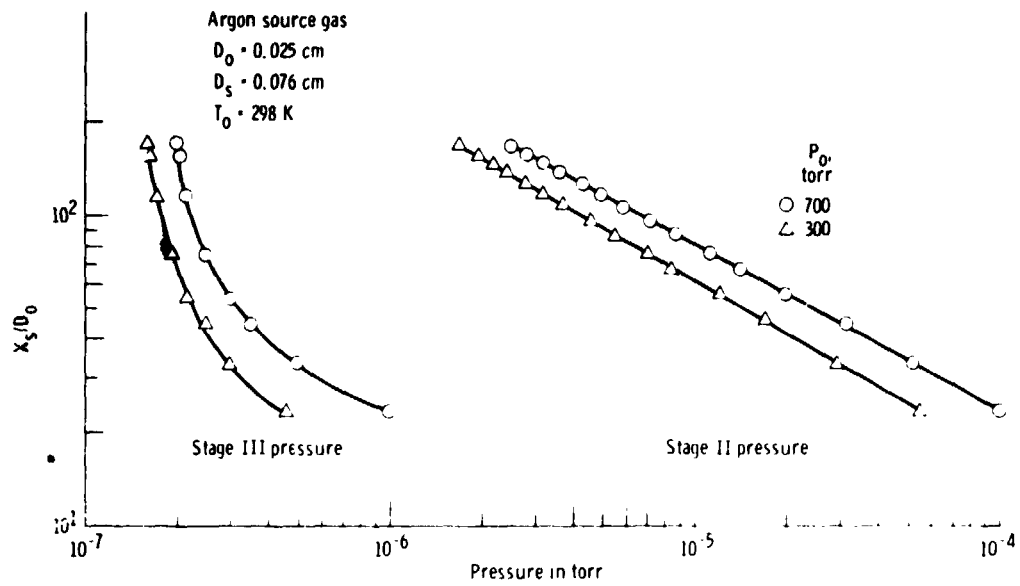


Figure 27. - Variation of second and third vacuum chamber pressures with orifice to skimmer distance at two source pressures.

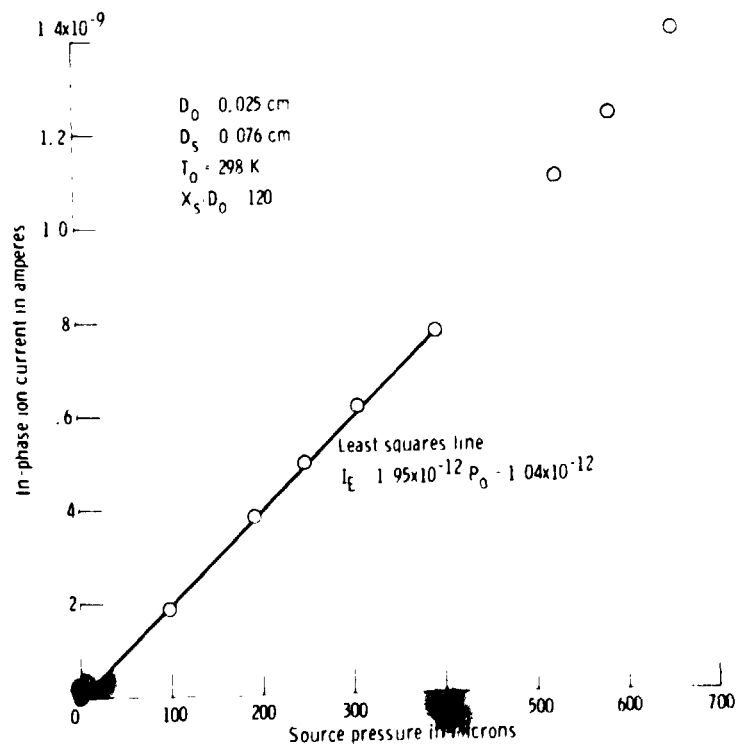


Figure 28. - Argon beam intensity as a function of source pressures in the effusive range.

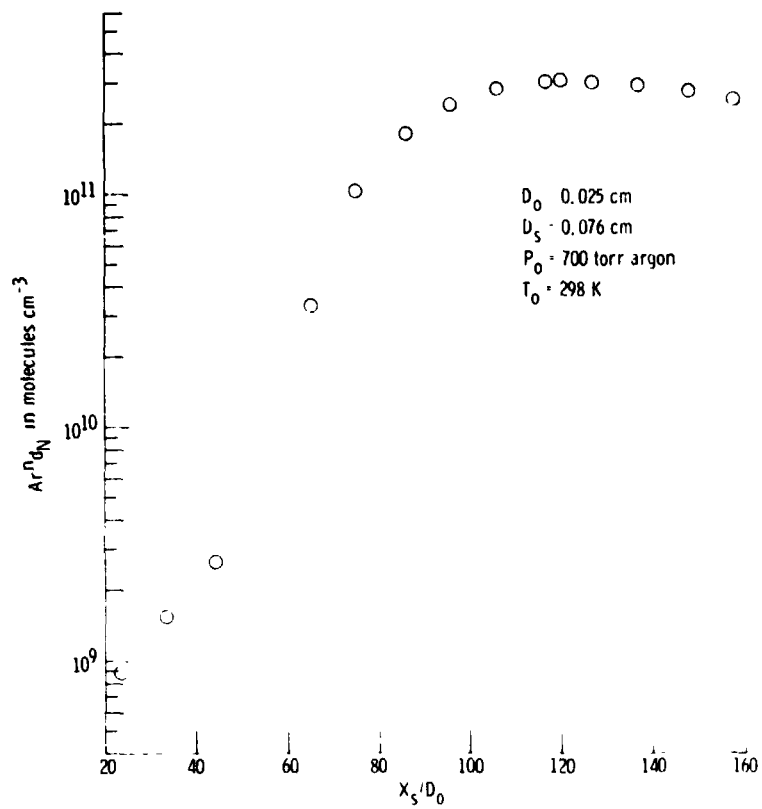


Figure 29. - Argon beam density at the detector plotted versus orifice to skimmer distance.

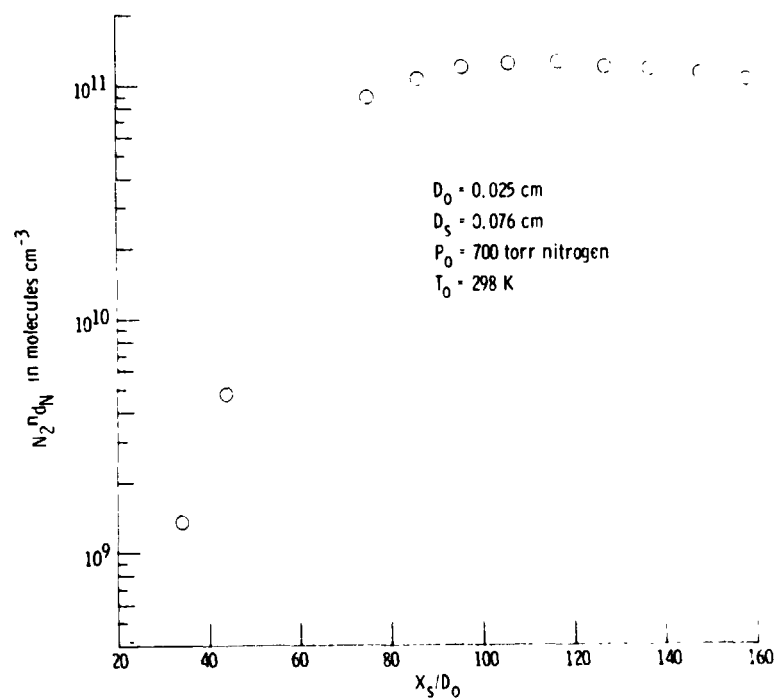


Figure 30. - Nitrogen beam density at the detector plotted versus orifice to skimmer distance.

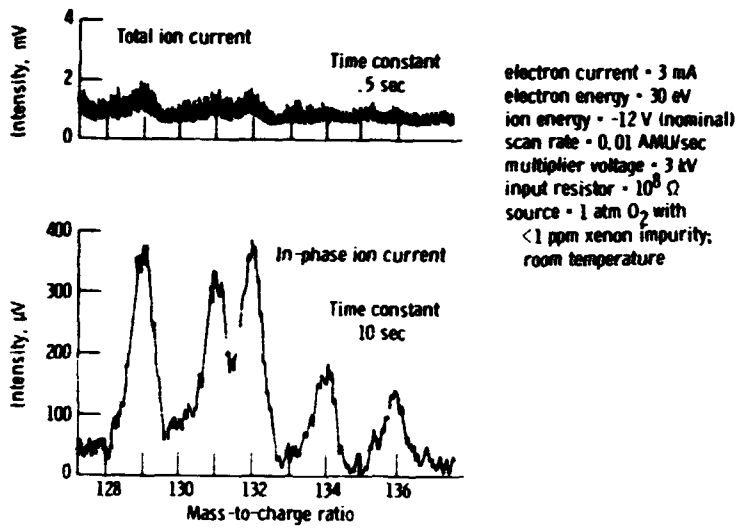


Figure 31. - Mass spectral scan of xenon isotopes

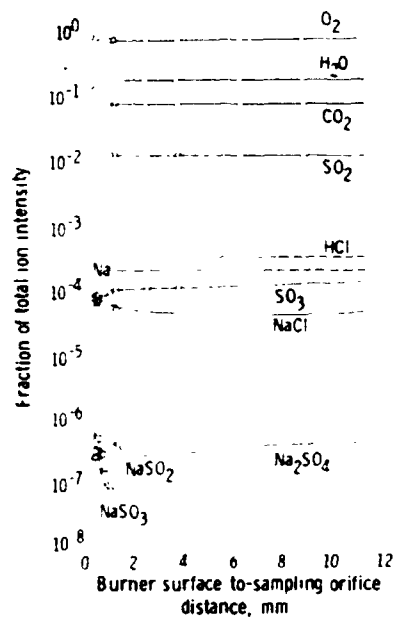


Figure 32. - Measured reaction product composition profiles for a methane-oxygen flame doped with  $SO_2 + NaCl + H_2O$ .

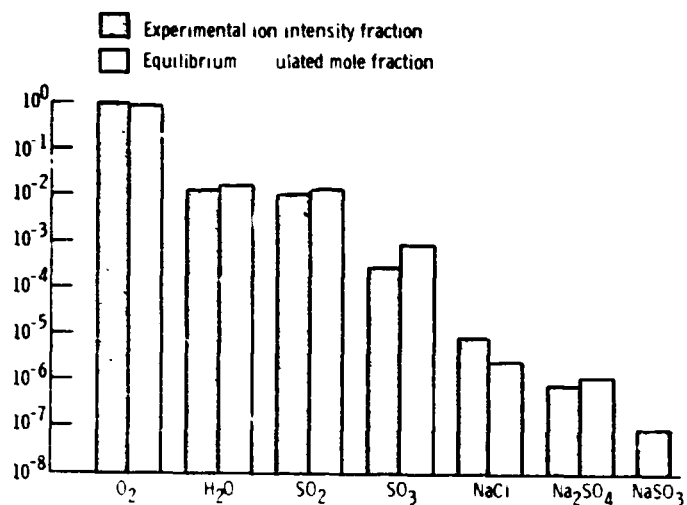


Figure 33 - Comparison of measured and equilibrium calculated reaction products produced at 1413 K in a flowing gas mixture of NaCl(l) + SO<sub>2</sub>(g) + H<sub>2</sub>O(g) + O<sub>2</sub>(g)

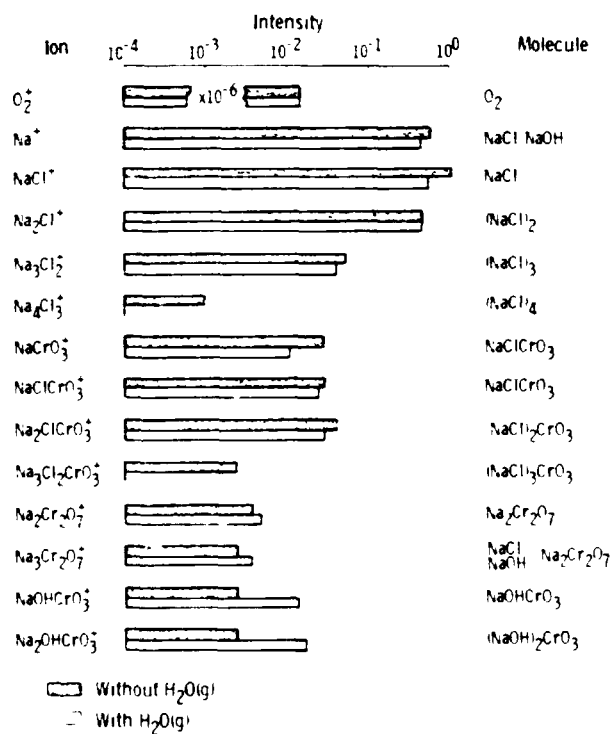


Figure 34 - Mass spectrum of vapors over Cr<sub>2</sub>O<sub>3</sub>(s) + O<sub>2</sub>(g) + NaCl(l) + H<sub>2</sub>O(g) at 1020°C